Spring 1987

A Simple Numerical Model for the Study of Baroclinic Estuarine Shelf Interactions

Thomas J. Berger
Old Dominion University

A SIMPLE NUMERICAL MODEL FOR THE STUDY OF BAROCLINIC ESTUARINE SHELF INTERACTIONS

by

Thomas J. Berger
A.B. June 1959, The Catholic University of America
M.S. April 1970, Naval Postgraduate School

A Dissertation Submitted to the Faculty of
Old Dominion University in Partial Fulfillment
of the Requirements
for the Degree of

DOCTOR OF PHILOSOPHY
OCEANOGRAPHY

OLD DOMINION UNIVERSITY
April, 1987

Approved by:

C.E. Grosch (Director)

Larry P. Atkinson

Shenn-Yu Chao

ABSTRACT

A SIMPLE NUMERICAL MODEL
FOR THE STUDY OF
BAROCLINIC ESTUARINE SHELF INTERACTIONS

Thomas J. Berger
Old Dominion University, 1987
Director: Dr. C.E. Grosch

A one and a half layer nonlinear f-plane numerical model was used to study estuarine-shelf interactions. The single active layer covered a domain consisting of a 100 *km* long by 20 *km* wide channel discharging onto a 100 *km* wide by 300 *km* long shelf. Channel and "western" shelf boundaries were no-slip, "eastern" or oceanic boundary was free-slip and "northern" and "southern" shelf boundaries were open. The channel was forced with a constant inflow velocity spun up from 2 $cm\ s^{-1}$ to 27 $cm\ s^{-1}$ over five days. The model initial conditions were a flat interface at ten meters and zero velocity except at the inflow. Effects of varying interfacial friction, Newtonian cooling (vertical mixing of density or detrainment), channel configuration and wind stress were examined. The principal result was to show that Newtonian cooling rather than interfacial friction played key role in deceleration and stagnation of an intrusion on the shelf relative to the constant phase speed in the channel. Deceleration of the density intrusion along the shelf coast agreed with results of three-dimensional numerical models, some laboratory models and with certain observed features of the Chesapeake Bay plume, for example. Results of a three-dimensional model were qual-

itatively reproduced as were features of a model which explicitly allowed the density interface to surface; that is, the plume flow was anticyclonic and marked by a region of supercritical flow along its outer edge. There was an abrupt transition, marked by strong nonlinear dynamics, from the plume to a coastal jet. Effects of channel configuration agreed with results of other models. Effects of wind stress were not adequately modeled probably due to failure to resolve the Ekman layer.

DEDICATION

To my wife Anne
and
my children Frederica, Catherine, Thomas and Andrea,
who made it possible.

ACKNOWLEDGEMENTS

I express my deepest appreciaton to my committee for their encouragement and support, both intellectual and material - to Dr. Shenn-Yu Chao for suggesting the topic and providing the computer code on which to build the model; to Dr. Larry P. Atkinson for providing the excellent facilities which made this modelling effort possible; and to Dr. Chester E. Grosch for providing the theoretical underpinnings for the work. I also thank the Computer Science Department for making the VAX available and reliable and Tad Guy for making UNIX comprehensible. The mistakes are, of course, my own.

TABLE OF CONTENTS

Page

APPENDICES

LIST OF FIGURES AND TABLES

Table

CHAPTER 1

INTRODUCTION

Density driven flows have attracted attention because of their theoretical and practical importance as fluid dynamics problems. Large estuaries influenced by the earth's rotation are special cases of such density driven flows. While not numerous, estuaries like the Chesapeake Bay are economically and ecologically important. Proper understanding of how these estuaries interact with the sea is important in fisheries and resource management, pollution control and waste disposal, recreation, navigation and shoreline management issues. They are, in addition, interesting from a purely scientific viewpoint. The general features of such flows include circulation patterns generated within the estuary, an adjustment region around the mouth - the near field - where the lighter water spreads out to form a plume, some form of jet like flow structure - the far field - along the coast and a region at the leading edge of the intrusion - the nose.

Analytical models, laboratory models and numerical models have all been used to study these important flows, but, because the processes involved are inherently nonlinear, they present difficulties for observationalists, theoreticians and numerical modelers alike. The theoretical and numerical approaches have involved linearizing the equations of motion and continuity and making other simplifications generally characterized as treating either the estuary or the shelf as a source or sink

of momentum or salt or as a specified sea level elevation and velocity profiles (tidal). Laboratory models can offer valuable insight into the processes involved but problems of hydrodynamic scales must be carefully addressed.

Numerical models do solve, in one sense, the mathemetical problems associated with nonlinear equations, but still leave concern about the correct interpretation of results. Numerical models can impose large computer time and memory requirements which make elaborate experiments difficult. Further, the conditions for numerical stability impose stringent limits on the dimension of the timestep for a given choice of grid spacing. In shallow coastal seas and estuaries the local baroclinic Rossby radius can be of the order of a few kilometers so the grid spacing must be small enough to resolve motions with this length scale. As a result the most restrictive condition for numerical stability is usually the Courant-Friedrichs-Lewy (CFL) condition that $\Delta t \leq \Delta x/c$ where $c = (g\,h)^{1/2}$ is the long wave phase speed. Experience with numerical models shows there is no *a priori* way to choose an appropriate timestep that otherwise meets the CFL condition. Timesteps which allow stable computation for some useful period in one model configuration may prove to be too large in another, as when wind is added. Two-dimensional models have the added drawback of disallowing the density interface to surface. Thus a prominent feature of density driven flows, the density front, cannot be duplicated.

Models of estuarine-shelf interactions which have included the effects of rotation and which examined the near field solutions are Beardsley and Hart (1978),

Ikeda (1984), Chao and Boicourt (1986), O'Donnell (1986) and Garvine (1987). A number of other workers have discussed far field effects, especially the nature of shelf break fronts, for example Kao (1981) and Csanady (1984). Still others have dealt with either interactions where rotation was not important (Garvine, 1982) or concentrated on estuarine circulations forced in some way by the shelf, Wang and Kravitz (1980), Wang (1985) and Spaulding (1984).

One approach to the problem has been to consider only the steady, linear part of the flow. This approach has the advantage of being more mathemetically tractable in that analytical solutions may be possible. Both Beardsley and Hart (1978) and Ikeda (1983) used steady state linear models with the estuary treated as a point source or sink. Beardsley and Hart (1978) focused on analytical solutions for a particular set of bottom profiles and considered the effect of a steady alongshore current in their two layer model. Ikeda (1983) considered only a flat bottom case with no ambient flow, again in a linear, steady state two layer model. Ikeda (1983) developed analytical solutions for the far field which he used as an asymptotic boundary condition for the near field solution. Both models produce anticyclonic flow in the upper layer near field with smooth transition to far field flow bound to the right hand coast. In both cases the anticyclonic flow was due to an upward sloping interface (looking seaward). Neither considered the effects of an applied wind stress or of tidal forcing.

Chao and Boicourt (1986) developed a fully nonlinear, time-dependent three dimensional (5 levels in vertical) model which included the estuary as a long

narrow channel entering the shelf at right angles. A rigid lid and flat bottom were specified to filter out coastally trapped barotropic wave components and to enhance the possibility of return flow in the lower layer. Their principal results were to show that the plume transition to a coastal jet is abrupt and is marked by strong cyclonic flow and downwelling while the flow within the plume is anticyclonic. Return flow is confined within the plume for reasonable values of vertical mixing and bottom drag. Flow in the coastal jet is unidirectional along the right hand coast. The density current or intrusion propagates much faster in the channel than on the shelf although the difference in speeds decreases as vertical mixing and bottom drag become small. Tidal mixing and wind effects were not considered. Chao and Boicourt (1986) attribute deceleration of the intrusion on the shelf to vertical mixing of both momentum and density.

Garvine (1987) has extended his previous work on small scale riverine discharges to the rotationally modified plume and its associated frontal dynamics in a steady state, nearly inviscid layer model. O'Donnell (1986) presented details of the development of this model and its application to time dependent cases of plume (near field) onset and growth. Garvine (1987) and O'Donnell (1986) used the method of characteristics to solve a layer model which explicitly allowed density fronts to develop and affect the dynamics of the plume. In this model a channel in geostrophic balance discharged onto a shelf with a specified ambient velocity. Even weak Coriolis force produced anticyclonic turning and a depth discontinuity type of density front. The turning region was characterized as having supercritical

flow (Froude number $U/C > 1$). The flow remained supercritical in cases of small outlet channel angle, or Kelvin number (ratio of channel width to Rossby radius of deformation) or both. For large angles and Kelvin number, the downstream flow reverted to a subcritical state and developed instabilities on the outer edge of the coastal jet.

Results of various laboratory models of density driven flows also showed deceleration of the current along the right hand wall. Whitehead and Chapman (1986) reported results of a laboratory model of a density current on a sloping shelf and attributed deceleration to radiation of barotropic waves from the nose of the intrusion. Results from the same tank experiment using a vertical wall, however, showed no appreciable slowing of the density current. Griffiths and Hopfinger (1983) attributed deceleration in a laboratory model with constant depth to radiation of momentum from the nose of the current in the form of inertial waves. Griffiths and Hopfinger (1983) also noted that the density intrusion decelerated continuously along the coast in their rotating tank model and eventually crept along the coastline via viscous expansion. Tank configuration in these laboratory experiments was not designed to examine the onset of an estuarine plume, however there was some indication of the plume and coastal jet configuration in Griffiths and Hopfinger's Figure 2c. This figure is similar to the numerical model results of Chao and Boicourt in that it shows the abrupt transition from plume to coastal jet.

The approach taken in this study has been to use a simple numerical model to examine the causes for deceleration and stagnation of the coastal jet. The simplest

approach to the dynamics which retains the density driven flow is a thin upper layer over an inert lower layer. The implication is that the two layers are effectively decoupled from each other and so can be evaluated independently. In particular the upper layer is decoupled from topographic effects. Is this reasonable in terms of physics? One effect of stratification is to inhibit exchange processes across an interface. Stable, i.e. $N^2 > 0$, stratification on a shelf is a characteristic of summer when solar heating and generally weak winds combine to establish a strong pycnocline. We are justified in using the single layer model to examine the dynamics of a stratified system if we restrict our interest to upper layer motions, that is the flow of lower density water onto a stratified continental shelf under the influence of earth's rotation, channel orientation and wind stress. This approach has the further advantage, beyond simplicity, that it is relatively economical of computer resources and so can be implemented on machines readily available to most researchers, in this case a VAX 11/785.

Linear theory predicts that forced motion in a channel will result in Poincaré and Kelvin wave propagation in the channel as the free surface attempts to maintain a quasi-geostrophic balance - the classic Rossby adjustment problem in a channel discussed by Gill (1977). If a rigid lid is imposed the same theory can be extended to wave motions on the interface between fluid layers of different density. The addition of corners to the channel induces additional effects which have been studied in terms of diffraction. Buchwald (1968) considered the case of diffraction of Kelvin waves at an inside corner (channel turns left in northern hemisphere) and

showed the generation of cylindrical Poincaré waves at the corner. Buchwald (1971) considered the diffraction of tides by a narrow channel. His results showed a Kelvin wave propagated into the channel and another Kelvin wave along the right hand coast. A standing Poincaré wave developed around the channel mouth as a matching solution. Webb and Pond (1986) extended this work to diffraction at an inside corner for arbitrary channel angles, widths and radii. For values comparable to this model, they predict almost complete transmission of energy around the corner in form of Kelvin waves. Cherniawsky and LeBlond (1986) examined steady state, nonlinear inviscid flow around arbitrary reentrant and inside corners using a perturbation expansion in terms of the Rossby number (U/fL). Addition of the terms of order of the Rossby number to the $O(1)$ geostrophic solution caused the current to widen at a reentrant corner which they attributed to the nonlinear terms.

Linear theory also predicts that phase speed will be constant in the channel and on the shelf. Chao and Boicourt (1986) found that the phase speed of a density current is faster in the channel than on the shelf. The question of whether this reduction in phase speed on the shelf is due to detrainment will be examined in this model by parametizing vertical mixing of density with a Newtonian cooling coefficient in the continuity equation. Newtonian cooling is a meteorological term used to parametize the long term effects of infrared radiation in driving the upper atmosphere to radiative equilibrium (Gill, 1982). In the oceanographic context it represents a change in volume due to vertical mixing of density.

The purpose of the present study was to examine the effects of mixing of density (entrainment/detrainment processes or Newtonian cooling) and mixing of momentum (interfacial friction or Rayleigh friction) on the character of the estuarine plume and coastal jet and on the propagation speed of the intrusion using a conventional reduced gravity model. The secondary purpose was to examine the applicablity of the approach to the entire flow regime from inflow at the head of the channel, adjustment to geostrophy and formation of the estuarine plume. The model explicitly allows examination of the predicted wave motions on that interface under various conditions of forcing. A major area of interest is the bay mouth region where there is an abrupt transition from the channel configuration which favors Kelvin wave propagation to a semi infinite ocean basin in which other wave modes are possible. The model differs from point source models in that the transition zone dynamics result explicitly from wave passage with no assumption of symmetry.

The principal result was that vertical mixing of density, as modelled by Newtonian cooling, was responsible for deceleration of the density intrusion on the shelf while vertical mixing of momentum controlled the rate of deceleration. For values of Newtonian cooling coefficient (ε) greater than $5.0\times10^{-6}\ s^{-1}$ the intrusion moved at constant speed in the channel but decelerated and eventually stalled at some distance downstream from the plume. For constant ε this distance was inversely proportional to the magnitude of the interfacial friction coefficient. For cases with ε small, the current moved at essentially constant speed in both the

channel and on the shelf. Wind effects have not been adequately modelled because the Ekman layer was not adequately resolved. Channel configuration effects were the result of Kelvin and Poincaré wave interactions with corners. The complex horizontal patterns of transition from plume to coastal jet seen in Chao and Boicourt's (1986) three-dimensional numerical model and in laboratory models were qualitatively reproduced by the two-dimensional model.

CHAPTER 2

THE MODEL

A one and a half layer nonlinear primitive-equation f-plane model was used. The combination of rigid lid and infinitely deep inert lower layer precluded any barotropic waves. Vertical mixing of momentum was parametized through linear interfacial friction. Vertical mixing of density was parametized through a Newtonian cooling coefficient in the continuity equation. In this context 'Newtonian cooling' represented a time constant for detrainment rather than a thermodynamic equilibrium constant as used in meteorology (Gill, 1982). After suitable manipulation of the transport equations for a two layer system, the model equations reduced to

$$U_t + L(U) - fV = -g^* h \eta_x + Ah\nabla^2 u + \tau^x - r_i u \tag{1}$$

$$V_t + L(V) + fU = -g^* h \eta_y + Ah\nabla^2 v + \tau^y - r_i v \tag{2}$$

$$\eta_t + \varepsilon\eta + U_x + V_y = 0 \tag{3}$$

where

L( ) is an operator defining the nonlinear terms,
g^* is reduced gravity,
η is the interface deviation from the initial condition,
$\tau^{x,y}$ is the wind stress,
r_i is the interfacial drag coefficient,
ε is the Newtonian cooling coefficient, and
subscripts t, x, and y indicate time and space derivatives.

Complete derivations for these equations are given in Appendix A.

Equations (1), (2) and (3) in three unknowns defined the lowest baroclinic mode of a two layer system. Since we have assumed the lower layer velocities to be zero, the equations described the dynamic fields in the upper, active layer.

The equations were cast in finite difference form and solved numerically using a staggered grid where pressure (interface depth) was computed at grid intersections and u and v were computed one half grid space to the left and one half grid space 'below', respectively, the pressure field. The code listing provided by Chao was that used by McCreary (1983) and represented a variation of Holland and Lin (1975) model. A complete program listing for the straight channel version is given in Appendix C. Coding of the nonlinear terms followed that of Holland and Lin (1975). Thus u was on a north-south and v was on an east-west physical boundary. Figure 1 shows the lower left corner of the grid. S, e and q represent h, v and u, respectively, at points one half grid space outside the boundary of the domain. These quantities were used in solutions of the continuity equation at the boundaries and in solution of the nonlinear terms which involve seventeen adjoining values of u, v and h. Values of h at these phantom points were found from solution of the momentum equations at the wall using Taylor series for the partial derivatives as shown in Appendix A. Equation (4) represents the momentum equation at a 'western' boundary with $h_0(=s_1)$ the value to be computed.

$$h_x = \frac{(h_1 - h_0)}{\Delta x} = \frac{fv_1}{g^*} + \frac{A}{g^*}\frac{(u_3 - 2u_2)}{\Delta x^2} + \frac{\tau^x}{g^* h} \tag{4}$$

This scheme allowed accurate specification of kinematic boundary conditions (no flow normal to the coast) on either east-west or north-south boundaries and simplifies coding of dynamic (free slip or no slip) boundary conditions. The coding used standard centered space and forward leapfrog time derivatives. Horizontal friction terms lagged the other terms by one timestep and were included for numerical stability. Vertical friction entered through wind stress and interfacial friction which acted as body forces on the upper, active layer. An Euler backward timestep was performed at a prime number (53) of timesteps to reduce the numerical mode splitting which occurs in leapfrog schemes. The model stored variables at three (n-1, n, n+1) timesteps except for the open boundary where a fourth time level (n-2) was needed at one grid point away from the boundary to solve the open boundary condition according to Orlanski (1976).

BOUNDARY CONDITIONS

Open boundary conditions were initially specified using the simplified scheme of Kreiss (1966), which assumed that the phase speed of any disturbance in the domain was just $\Delta x/\Delta t$. The simplified condition worked in the shelf model configuration but not in the bay shelf configuration. The final radiation condition used was the Orlanski (1976) radiation condition in a form suggested by Chapman (1985), in which the phase speed of each quantity (u,v,h) was calculated and applied in determining the future (n+1) value of the quantity on the open boundary. While this formulation allowed different propagation speeds for each property it also had the restriction that c_ϕ where ϕ was the specified property, must be in the range $0 \leq c_\phi \leq \Delta x/\Delta t$. The minor disadvantage of this condition was that it required a value away from the boundary at a fourth (n-2) timestep.

Physical boundaries in the model, i.e. the channel walls and the western boundary of the shelf, were treated as no-slip walls ($u = v = 0$). The eastern (oceanic) boundary was specified as free slip ($u = 0$, $v_x = 0$). The presence of the channel added an inside (convex) corner where the channel entered the shelf as shown schematically in Figure 1. The value of the interface height outside the grid (marked s* in Figure 1) used in solving the momentum equations was treated, following Roach (1976), as being double valued. Thus the value of s* in Figure 1

Figure 1. Staggered Numerical Grid. Points marked q, e and s represent u, v and h at grid points outside the physical boundaries. Heavy line marks the physical boundary.

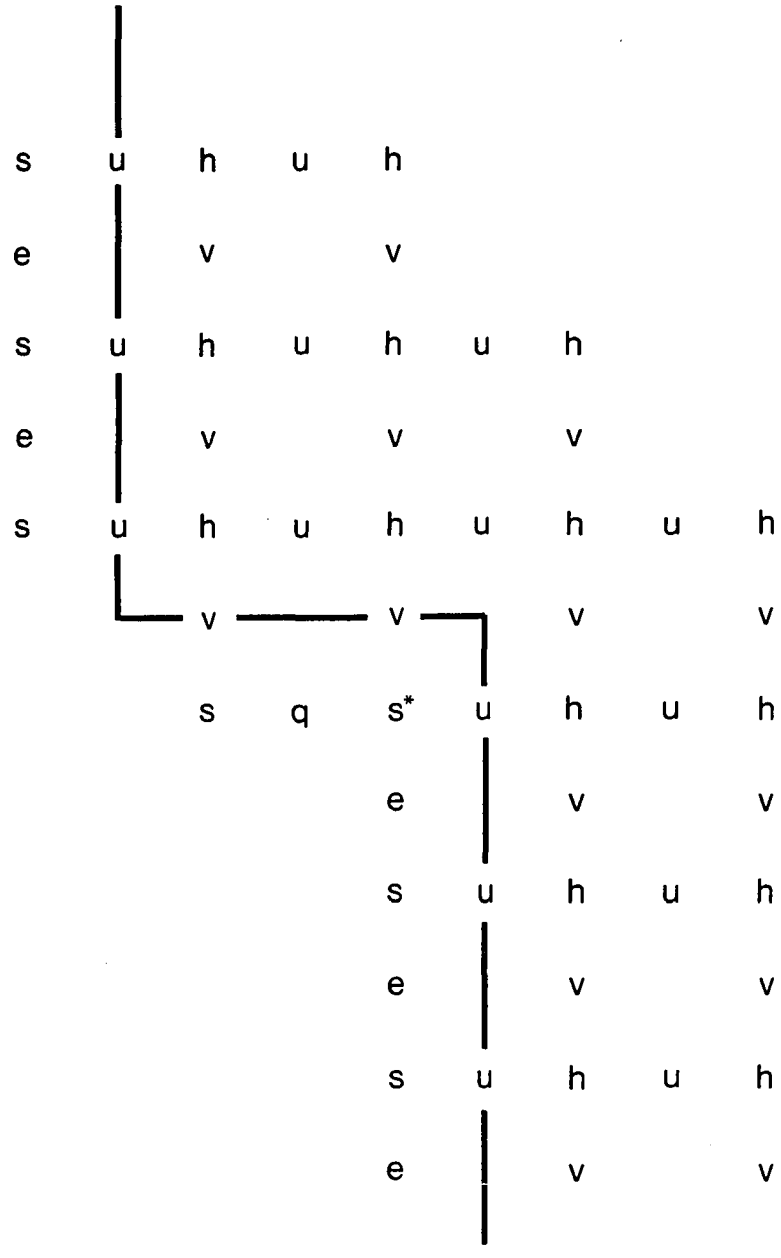

was obtained from a solution of the x-momentum equation for values used in computing u and from solution of the y-momentum equation for values used in computing v.

Wind stress was the product of a patch function wf(y) and component ($\tau^{x,y}$) magnitude and was constant in direction for a given experiment. The patch function was zero within 30 *km* of northern and southern boundaries, ramped up(down) for 10 *km* and was constant (wf=1) over the remainder of the domain. The result of using the patch function was that the wind stress curl was everywhere zero except in the area covered by the ramp and only when τ^x was non zero. The wind was either ON for a specified time or OFF and had a non zero component in x or y direction.

NUMERICAL INTEGRATION

The finite difference equations were integrated over the model domain with grid spacing of 2 *km* in both x and y directions. Distance along the right hand channel wall (looking downstream) was 100 *km* in all model configurations. A 200 *km* coast downstream of the estuary mouth allowed examination of the coastal jet for reasonable periods. Timestep was 300 seconds which satisfied the CFL condition for numerical stability. The constant value of reduced gravity was 2.0 $cm\ s^{-2}$ which corresponded to a constant density difference of 2 σ_t units. Model initial condition was a flat interface at 10 *m* and zero velocity everywhere except the head of the channel where $|u,v| = 2.0\ cm\ s^{-1}$. The inflow velocity at the head of the channel was increased over 5 days to 27 $cm\ s^{-1}$ using a tanh function to damp any inertial oscillations and so promote numerical stability. The maximum value of the inflow was of order $10^5\ m^3 s^{-1}$. The inflow was approximately half the mean outflow from the Amazon ($1.75 \times 10^5\ m^3 s^{-1}$, Gibbs, 1970) and two orders of magnitude greater than estuaries such as the Columbia River and Chesapeake Bay ($2039\ m^3 s^{-1}$, Boicourt, 1973). Initial experiments showed that the model results were not sensitive to the magnitude of the inflow. The value chosen allowed things to happen in a reasonable time period.

The range ε used in this series of experiments was 0.0 to $1.0\times10^{-5}\ s^{-1}$. The maximum value of ε was that which kept all the terms in the continuity equation of O (1). Horizontal mixing of momentum was included only to ensure numerical stability. Vertical mixing of momentum was included in the form of linear interfacial friction coefficient that ranged from 0.0 to 0.035 $cm\ s^{-1}$ and in some experiments in the additional form of wind stress of 0.5 $dynes\ cm^{-2}$.

Model runs were typically ten model days duration. Interface height ($h - h_0 > 10.0\ cm$) was contoured at two meter intervals and velocity vectors ($|u| > 1.0\ cm\ s^{-1}$) plotted every model day. Velocity components and interface height were stored at the end of each run for use in restarting the model and for data analysis. Daily interface height contours were used to track nose position of the intrusion which was arbitrarily chosen as the location of the two meter isopleth measured approximately two kilometers from the right hand wall. Velocity vectors were computed at the same grid position as the interface height. For clarity only every other vector was plotted. Time and length scales for the exponential decay of the coastal jet were computed using the method of Mangelsdorf (1959) for unknown asymptotes.

Experiments were designed to determine the effects of Newtonian cooling and interfacial friction in the straight channel case and to examine the effects of channel orientation and wind forcing using fixed values of ε and interfacial friction. The three channel orientations included one normal to the coast (T) and two parallel to the coast (L and Γ). The two orientations parallel to the coast covered the case (L)

where northward, upwelling favorable winds retarded the flow on the shelf and and in the channel; and the case (Γ) where northward, upwelling favorable wind accelerated flow in the channel and retarded flow on the shelf. A series of preliminary experiments was conducted to determine the behavior of the model with different forcings, frictional parameters and velocity spin up times. A brief series of complementary experiments on a 100 *km* by 200 *km* shelf were also conducted.

CHAPTER 3

NUMERICAL RESULTS

Numerical results on the effects of Newtonian cooling and interfacial friction in the straight channel case are presented first, principally in terms of experiment T1. Following the discussion of the straight channel case, results for the two other channel orientations are presented and compared with the straight channel. Finally, effects of constant wind stress applied for three days are presented. Figure 2 outlines the domain for the straight channel case. Points where measurements were taken are marked with arrows. Table 1 lists the model variables for each experiment along with computed nose propagation speeds, penetration lengths and decay times.

Within six hours of start time the intrusion began to turn anticyclonically until it reached the right hand channel wall. There it turned cyclonically and propagated along the wall. The interface deepened on its right side and had the appearance of a thinning wedge as it propagated along the wall. The interface continually deepened at the head of the channel under the influence of increasing inflow, which reached steady state condition at about day six in versions with Newtonian cooling. Other versions showed no evidence of steady state before the end of the experiment (T6) or before becoming numerically unstable (T3, T5). All the versions had similar appearance in a vertical along channel section and the experiments with

Figure 2. Model Domain. (a) T or straight channel, (b) L and (c) Γ. Dimensions in kilometers. Small tick marks indicate locations where current width measurements were taken in channel and on shelf. Open arrow indicates inflow. Channel walls and western shelf boundary are no-slip. Eastern boundary is free-slip. Shelf in each figure is 100 *km* by 300 *km*. Channel is 20 *km* wide and 100 *km* along the right hand wall in each case. "Open" indicates shelf boundary with radiation boundary condition.

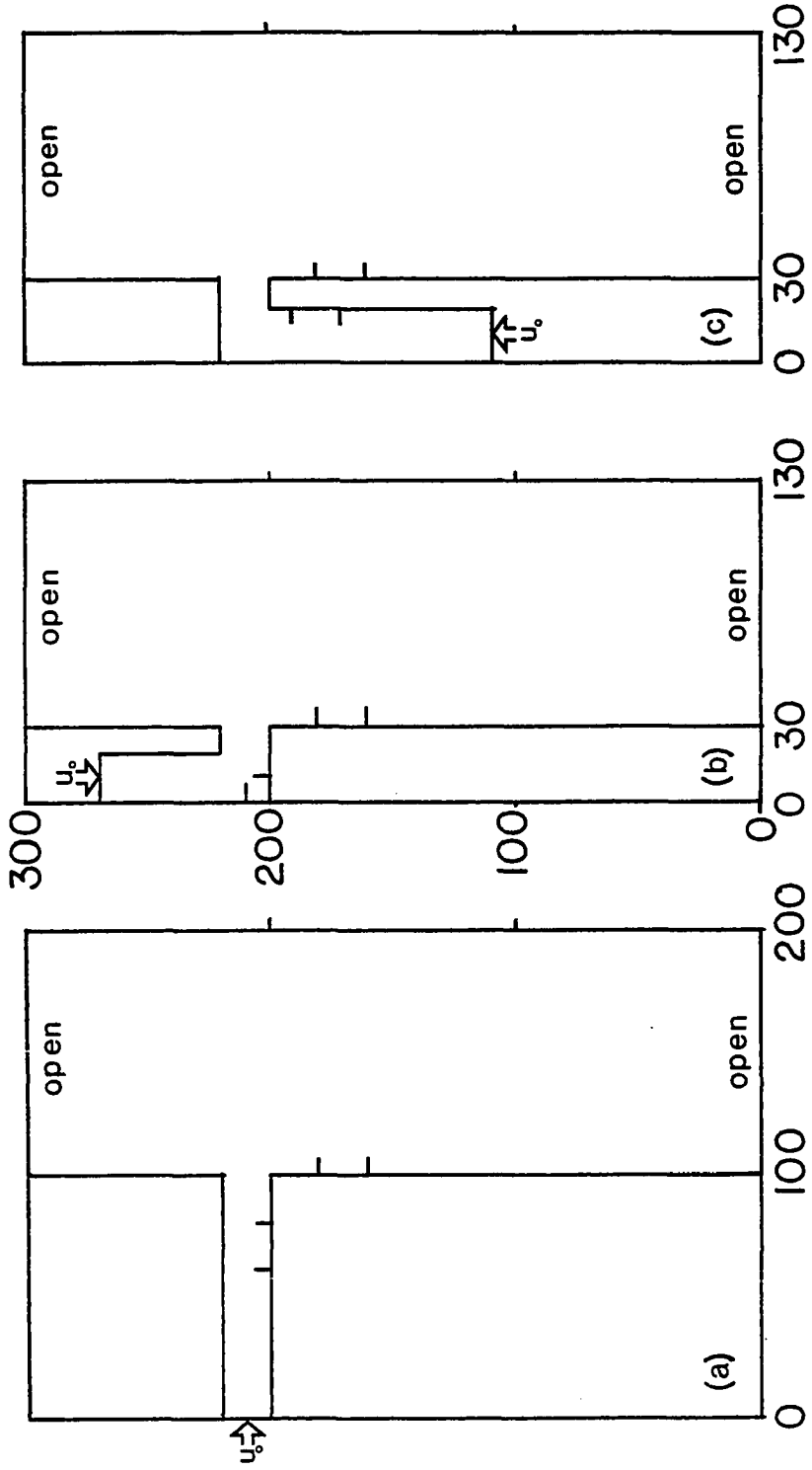

Table 1. Experiment Parameters

Case	Parameters		Penetration Length		Decay Time		Propagation Speed		
	ε	r_i	L_{p_c}	L_{p_s}	α_c	α_s	C_c	C_T	C_s
T	1e-5	0.0350	112.1	21.5	-0.257	-0.480	19.3	10.6	5.9
T1	1e-5	0.0035	111.7	117.3	-0.400	-0.302	34.5	6.9	14.3
T2	1e-5	0.0070	110.1	96.2	-0.347	-0.315	32.5	18.1	12.2
T3	0e0	0.0	119.6	-1302.7	-0.537	0.028	44.3	44.3	46.0
T4	1e-5	0.0	108.4	172.8	-0.289	-0.246	36.5	24.6	18.8
T5	0e0	0.0035	121.6	-3773.8	-0.680	0.010	42.9	42.9	44.1
T6	1e-6	0.0035	119.0	-18143.2	-0.574	0.002	41.8	41.8	42.4
T7	5e-6	0.0035	111.3	385.2	-0.307	-0.111	37.0	31.4	27.5
L1	1e-5	0.0035	115.7	167.3	-0.533	-0.803	35.5	19.6	22.7
L5	0e0	0.0035	115.8	-985.0	-0.527	0.039	46.5	46.5	53.0
Γ18	1e-5	0.0035	85.2	432.9	-0.387	-0.081	34.5	30.0	27.2
Γ110	1e-5	0.0035	106.3	327.6	-0.315	-0.110	36.5	21.3	24.4
Γ5	0e0	0.0035	113.6	-1144.0	-0.757	0.033	45.2	45.2	50.5

Notes:

- All experiments had constant $f = 1.0\times10^{-4}\ s^{-1}$, $g^* = 2.0\ cm\ s^{-2}$ and $A_H = 3.0\times10^5\ cm^2\ s^{-1}$.
- Case Γ18 indicates experiment with 80 *km* distance along right hand channel wall. All other experiments had 100 *km* distance along right hand channel wall.
- Subscripts c and s indicate data for channel and shelf respectively.
- C_T indicates propagation speed computed from linear regression of all nose position data versus time for a given experiment.

small ε were consistently deeper, as expected. Plan view of the interface showed a more jet like appearance in experiments with small ε but neither version had any notable structure in the region of the nose.

At the channel mouth the intrusion began immediately to turn right along the coast under the influence of the Coriolis parameter and to expand slowly in the offshore direction. In all cases with ε greater than $5.0\times10^{-6}\ s^{-1}$, except T, the intrusion reached the channel mouth at about day three. For experiments with small or zero ε the intrusion reached the mouth about one day earlier. As time continued a bulge or plume characterized by anticyclonic turning developed in the first 20 *km* downstream from the channel mouth. This plume expanded very slowly in the offshore direction and deepened along the right hand wall. In general the deepest part of the plume was slightly downstream of the widest part of the plume. In most cases the flow separated from the wall as evidenced by the formation of a complete anticyclonic gyre within the plume.

A coastal jet appeared almost immediately after the flow rounded the corner and propagated along the right hand coast as the plume expanded in volume. Width of this jet appeared to be constant for most of its length. Those with small ε were much wider and had a pronounced lateral indentation near the plume. The nose in experiments with small ε (T3, T5 and T6) showed evidence of wave like structure on the offshore edge and appeared to have a steep vertical profile immediately behind the nose. Figure 3 illustrates the interface height and velocity vectors in this progression for model version T1 from day three to day six. Figure 4

Figure 3. Interface Contours and Currents. Model version T1 with $r_i = 0.0035\ cm\ s^{-1}$ and $\varepsilon = 1.0 \times 10^{-5}\ s^{-1}$. Interface depth $(h - h_0)$ for (a) day three, (c) four, (e) five and (g) six. Contour interval of 200 cm. Currents shown in (b), (d), (f) and (h) for days three through six. Length of maximum vector is constant shown by arrow. Figures show propagation of intrusion from near mouth of channel and around corner, formation of plume and coastal jet.

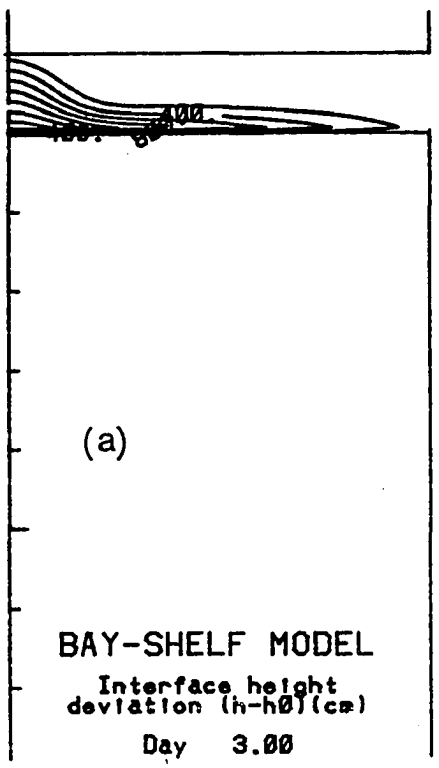

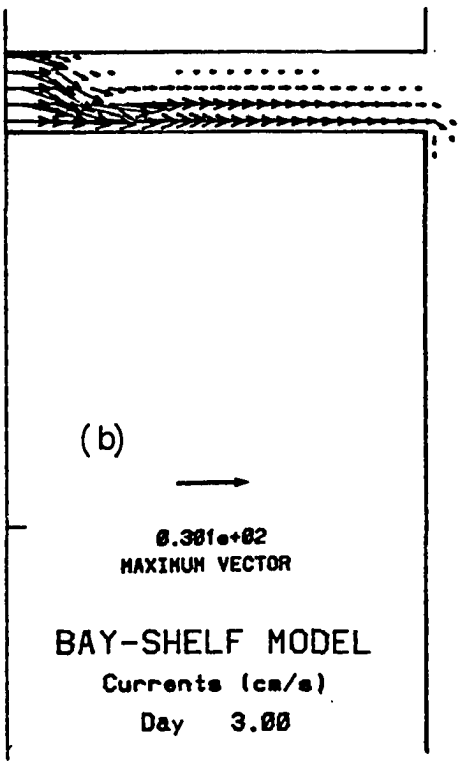

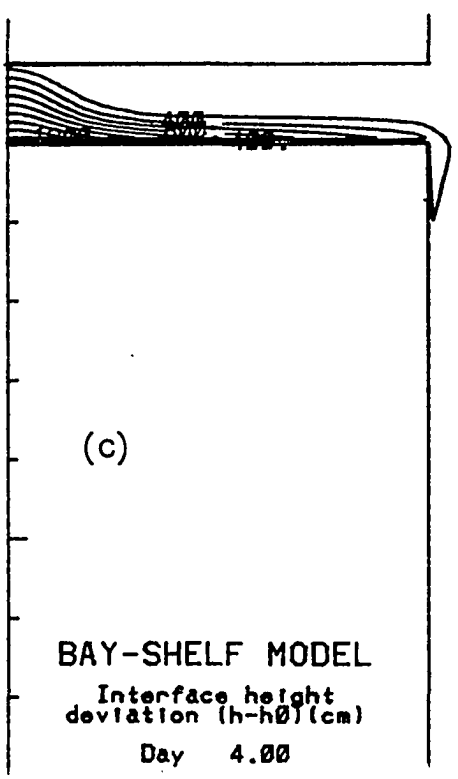

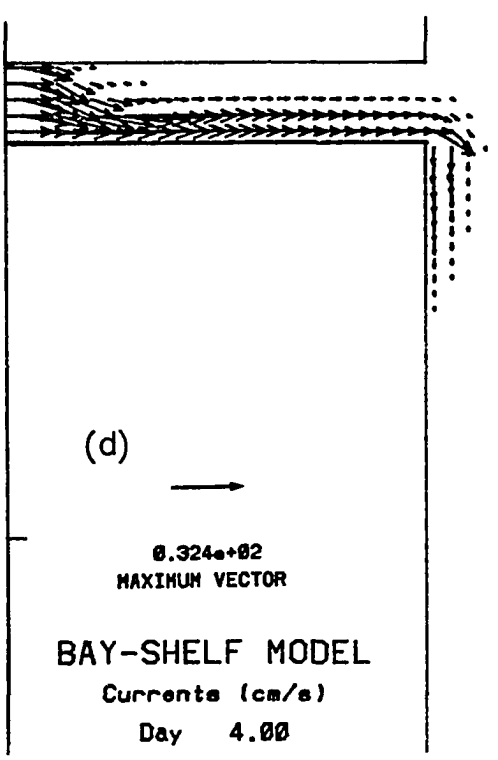

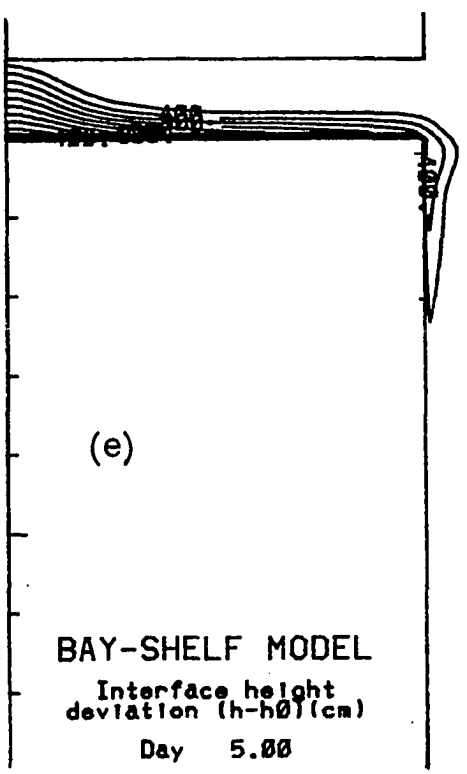

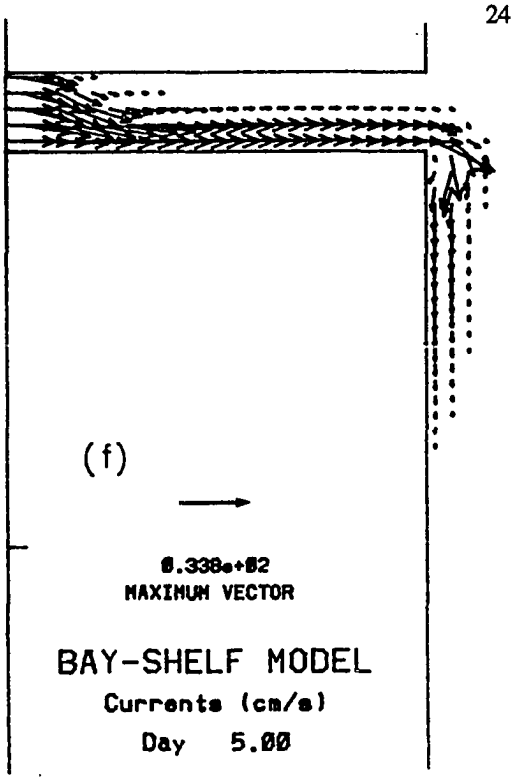

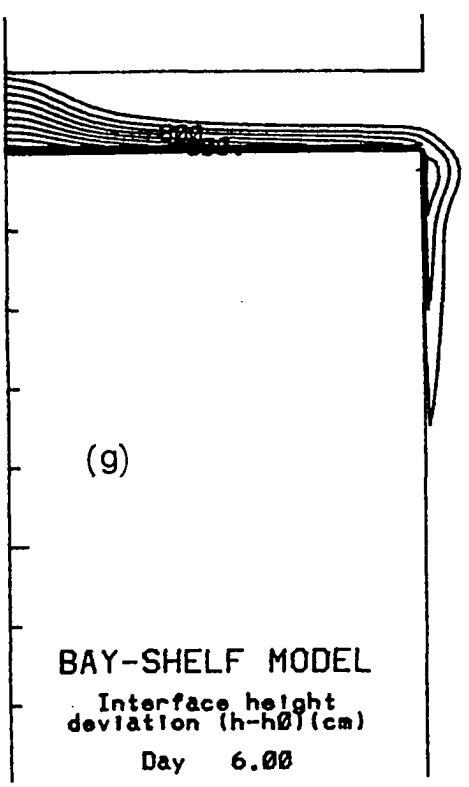

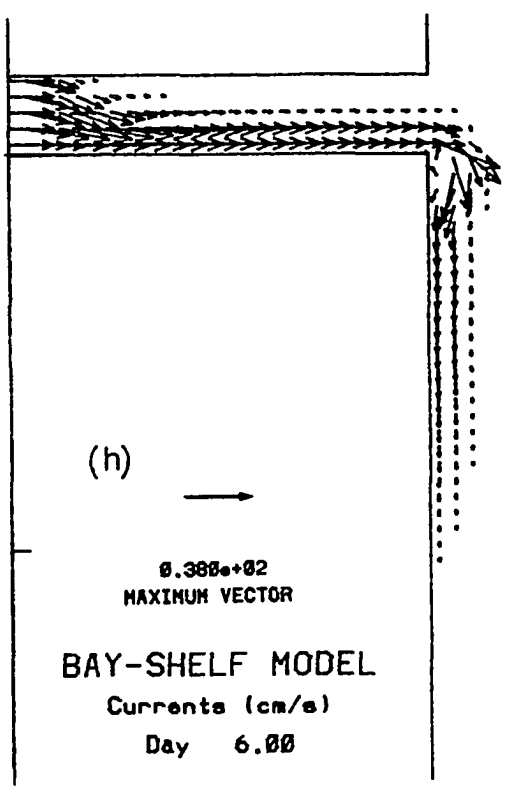

Figure 4. Interface Contours and Currents. Model version T6 with r_i=0.0035 $cm\ s^{-1}$ and $\varepsilon = 1.0\times10^{-6}\ s^{-1}$. (a) Interface depth $(h-h_0)$ contours at 200 cm intervals and (b) current vectors on day six.

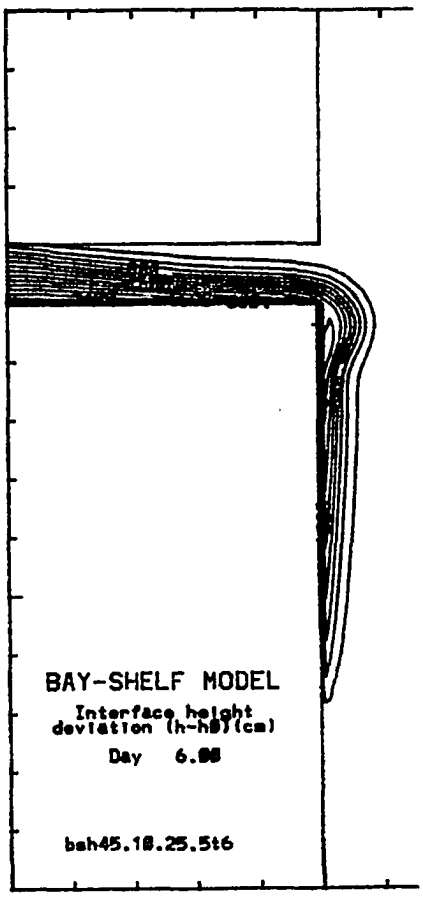

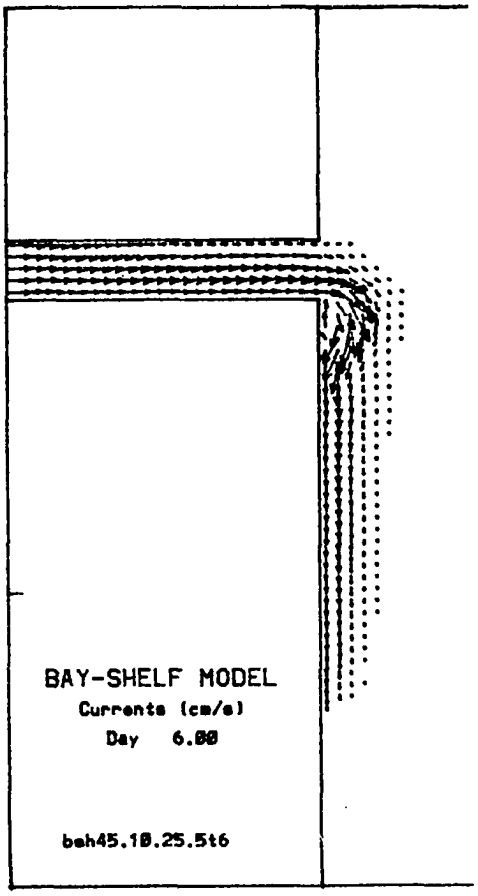

shows the depth contours and currents for version T3 on day six.

Initially the maximum velocity was found near the head of the channel but as time progressed the locus of the maximum velocity moved downstream, consistent with rotational acceleration of the density current in the channel. Width of the velocity structure matched the appearance of the interface in the channel, being jet-like for experiments with large ε and broader in experiments with small ε. Once the plume developed, the maximum velocities were found in the plume at the channel mouth. The experiments with large ε show evidence of a small cyclonic gyre or counterflow at about the two o'clock position on the outer edge of the plume. This feature was not seen in any version with small ε. It was also absent from a linear version and one in which the channel width was ten kilometers.

Velocity in the coastal jet decayed downstream from the plume in all versions, but those with small ε appeared to decay much more slowly, if at all. Maximum velocities in the coastal jet were less than half the maximum in the plume for versions with large ε and approximately 70 percent of the maximum in the plume for the other versions. In any case maximum velocities in the plume were inversely proportional to the value of ε. Significant cross stream velocities were found only in the inflow region and in the plume in the versions with large ε. Experiments with negligible detrainment exhibited virtually parallel flow in the channel even at the head of the channel, cross stream flow in the plume and confused flow patterns at the offshore edge of the nose.

EFFECTS OF INTERFACIAL FRICTION AND DETRAINMENT

Nose Propagation Figure 5 shows the nose position (X_N) for the first ten days of all model experiments plotted versus time. This figure shows qualitatively that the nose of the jet has decelerated (or stalled) along the shelf boundary in the experiments with ε greater than $5.0\times10^{-6}\ s^{-1}$ while propagation speed appeared nearly constant in the experiments with smaller values of ε. The solid line indicated by C_0 shows nose position due to the linear propagation speed. The four straight channel experiments with constant ε ($1.0\times10^{-5}\ s^{-1}$) and different values of interfacial friction showed propagation speed apparently less than the linear wave speed, higher in the channel than on the shelf and decelerating on the shelf. Experiment T7 with smaller ε ($5.0\times10^{-6}\ s^{-1}$) gave comparable results in that the coastal jet stalled along the coast. Two experiments with no Newtonian cooling and different values of interfacial friction (0.0 and 0.0035 $cm\ s^{-1}$) showed no evidence of deceleration on the shelf for the duration of the experiment. Both experiments become numerically unstable before ten days for reasons apparently related to the open boundary condition. A third experiment (T6) with smaller ($1.0\times10^{-6}\ s^{-1}$) ε had a similar result with slightly lower propagation speed.

Linear regression of nose position versus time was made to estimate the nose propagation speed for each experiment. If linear theory holds the expected result

Figure 5. Nose Position versus Time. Daily nose position for 13 experiments (X_N = distance from head of channel in kilometers) versus time in days. Line indicated by C_0 is position of an intrusion moving at linear wave speed. Dotted lines are experiments with $\varepsilon > 5.0\times10^{-6}\ s^{-1}$, dashed lines are experiments with $\varepsilon = 0.0$ *or* $1.0\times10^{-6}\ s^{-1}$.

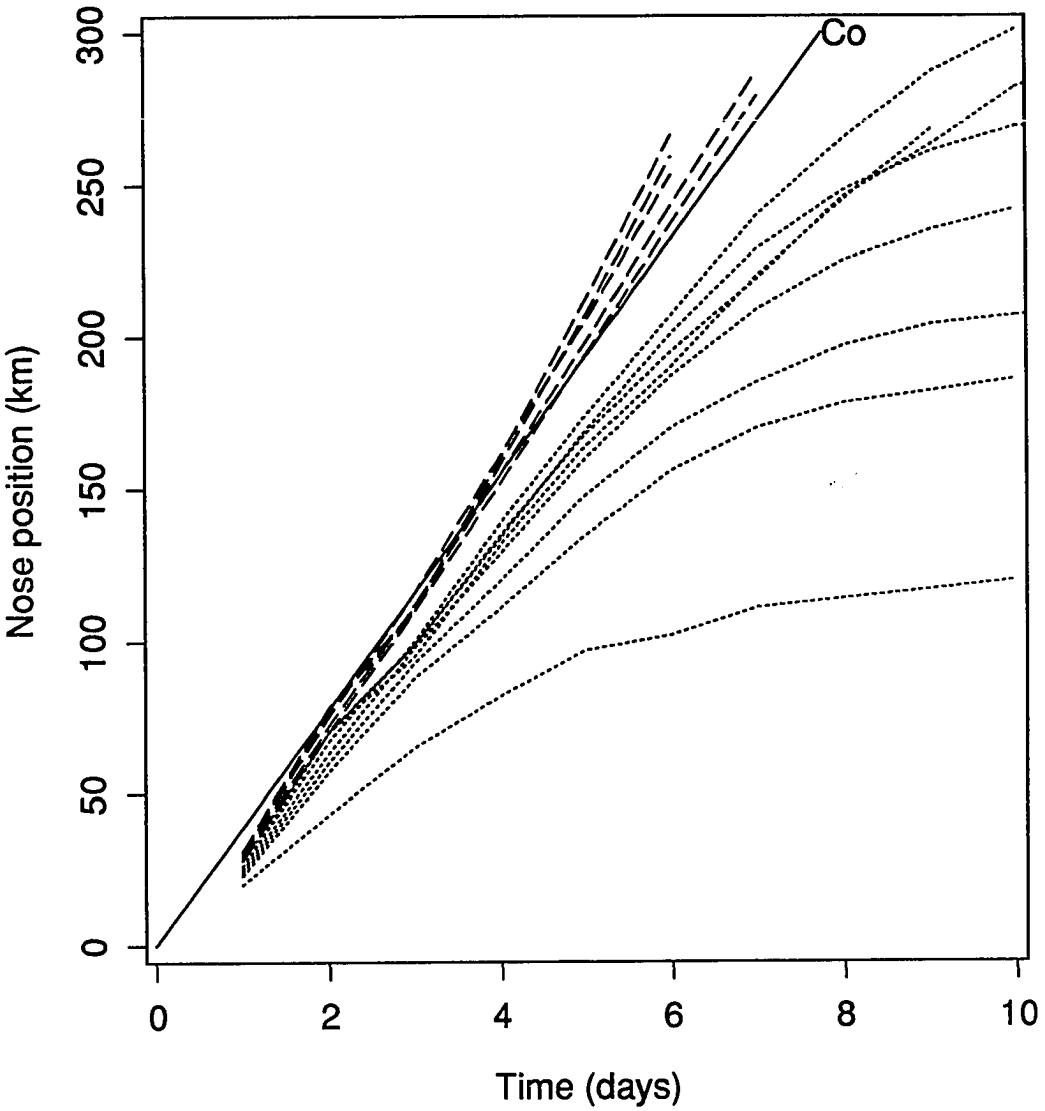

would be that the slope of the line divided by the linear phase speed should be approximately 1.0. The experiments with larger ε gave mean propagation speed in the channel $\overline{C}_c = 31.96\ km\ d^{-1}$ ($\overline{X}_N = -7.24\ (km) + 31.96\ (km\ d^{-1})\ t(d)$) using the means of the intercept and the slope. Correlation coefficients were greater than 0.991 and the ratio of the mean slope to the linear propagation speed ($\overline{C}_c/C_0$) was 0.827. Use of all data points for these experiments, i.e., nose positions in both channel and on the shelf, gave $\overline{X}_N = 40.74 + 18.32\ t$ with correlation coefficients in the range from 0.556 (T1) to 0.987 (T7) and $\overline{C}/C_0 = 0.474$. In this case the positive intercept indicated a physically unrealistic result, namely propagation of the intrusion prior to start of the experiment. As a further check on propagation in the channel experiment T1 was rerun to allow determination of nose position at six hour intervals. These data gave $X_N = -9.75 + 34.27\ t$ ($C_c = 34.27\ km\ d^{-1}$) with correlation coefficient of 0.999.

Fit of the nose position versus time (all data points) for three experiments (T3, T5 and T6) with small ε gave a mean nose position $\overline{X}_N = -14.86 + 43.01\ t$ with correlation coefficients greater than 0.999 and $\overline{C}/C_0 = 1.113$. Since daily nose positions gave too few points for determination of the propagation speed in the channel for these experiments, T6 was rerun and nose position in the channel determined at six hour intervals. These data gave $X_N = -15.00 + 42.80\ t$ and correlation coefficient of 0.999. The value for propagation speed in the channel was not significantly different from the mean determined from all the data and I conclude that the propagation speed was constant in these versions and greater than linear

propagation speed. Propagation speeds greater than linear wave speed have been shown by Bennett (1973) for Kelvin waves to be caused by the advective terms in the momentum equations. Experiments with linear versions of the model showed that the nonlinear terms increased the phase speed by about 2.9 percent.

Another estimate of nose propagation speed was obtained by dividing daily nose position by elapsed time. Figure 6a shows this nose propagation speed normalized by linear phase speed plotted against time normalized by inertial period ($T_i = 2\pi/f$). Figure 6b shows normalized propagation speed plotted against nose position normalized by Rossby radius of deformation (X_N/R_0). The experiments with small ε were at least qualitatively different from those with larger ε in that they did not appear to be decelerating whereas the others do. All the experiments indicated rapid acceleration in the first day of the experiment and deceleration as the intrusion neared the mouth of the channel. Interval by interval calculations of propagation speed showed the same trends but with more scatter in the data. Polynomial regression of these data with and without the first point gave correlation coefficients from 0.846 to 0.949 (all points) and from 0.961 to 0.999 (all points less first) with all but one greater than 0.980.

Linear regressions of propagation speed versus both ε and interfacial friction showed that propagation speed in the channel for all experiments was about equally correlated with ε and with interfacial friction ($C(\varepsilon) = 44.2\ km\ d^{-1} - 12.8\,\varepsilon$ and $C(r^*) = 39.94\ km\ d^{-1} - 6.98\,r^*$) with correlation coefficients of 0.63 and 0.48, respectively. Taking only values of propagation speed when either ε or interfacial

Figure 6. Nose Propagation Speed. Daily computation of nose speed ($C = X_N/t$) normalized by linear propagation speed C_0 plotted versus (a) time normalized by rotational period ($T_i = 2pi/f$) and (b) nose position normalized by Rossby radius. Arrows in (a) indicate asymptotic velocity U_0 computed by Griffiths and Hopfinger (G&H) and Stern, *et al.*, (S). Solid line is linear fit to data from experiment T6. Dotted lines indicate experiments with $\varepsilon > 5.0\times10^{-6}\ s^{-1}$, dashed line indicates $\varepsilon = 0.0\ ,\ 1.0\times10^{-6}\ s^{-1}$.

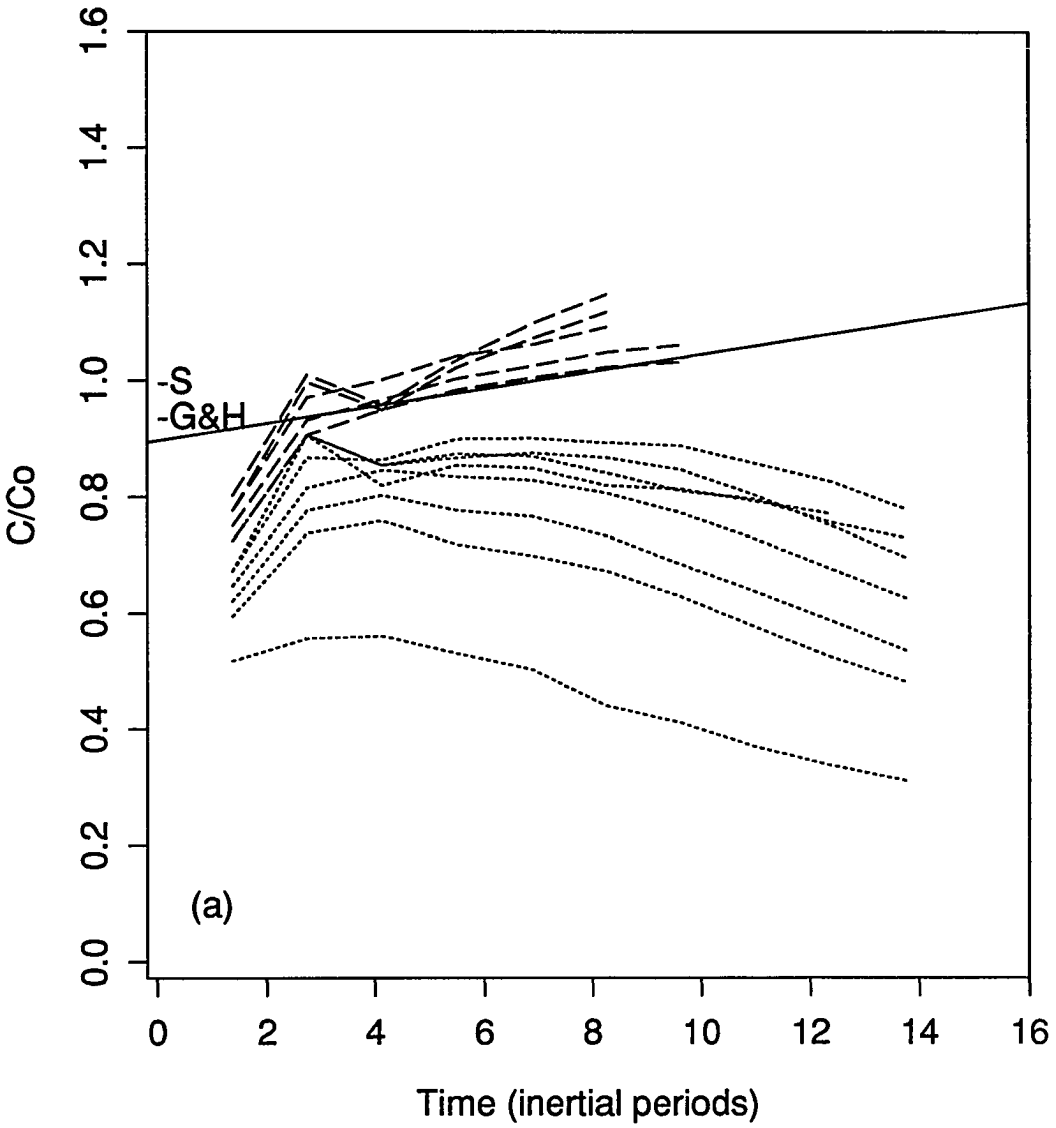

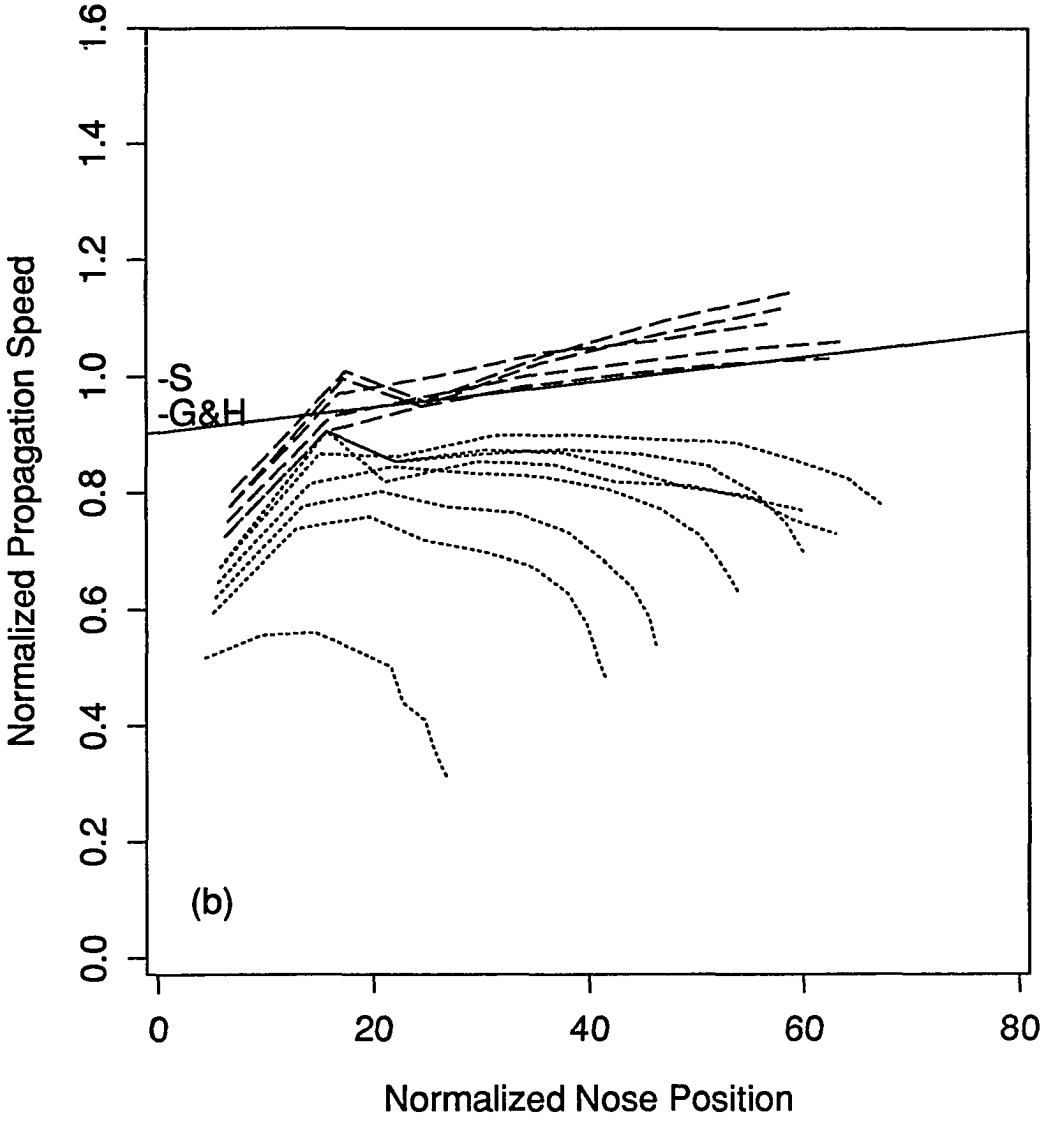

friction was constant made only a small improvement in the correlations. Regression of all the data for both channel and shelf gave $C = 44.7\ km\ d^{-1} - 30.8\ \varepsilon$ with correlation coefficient of 0.84. The same values of propagation speed were essentially independent of interfacial friction. Regressions were also made against the sum of ε and interfacial friction and against the square root of their product. Channel speed was reasonably correlated with both (correlation coefficients of 0.80 and 0.79), but propagation speed based on channel and shelf data was not well correlated with either sum or product.

Asymptotic Behavior of the Nose Time and distance scales for the decay of the current, decay time (α) and penetration length (L_p), respectively, were computed in two separate regimes, the channel and the shelf, to further explore the apparent differences in propagation between channel and shelf.

Penetration length computed in the channel extended seaward of the estuary mouth and was nearly constant in the cross shelf direction regardless of the magnitude of interfacial friction but appeared to be reasonably well correlated with ε (correlation coefficient of 0.852 for all data and 0.764 for data with constant interfacial friction). Decay time was less strongly correlated with detrainment (correlation coefficients 0.737 and 0.560, for same cases as penetration length). In all eight straight channel cases the decay time was negative in the channel regime. Lower correlation coefficients for decay time may be due to the method of computation.

Penetration length and decay time along the shelf were poorly correlated with

interfacial friction. In the absence of detrainment the intrusion had negative penetration length and positive 'decay' time which indicated a process that was growing rather than decaying. The negative penetration length had no physical significance. In fact both of these experiments became numerically unstable in a manner consistent with rapidly growing velocity or with upstream propagating waves. The numerical instability could result from such waves since the open boundary condition allows only propagation out of the domain. The experiment with small ε ($1.0\times10^{-6}\ s^{-1}$) also exhibited this growth mode but the time constant was of the order of several hundred days. This experiment remained numerically stable. Garvine's (1987) nearly inviscid, steady state model produced downstream-growing unstable disturbances embedded in the coastal jet. The phenomenon must be related to the time-growing disturbances produced here.

Griffiths and Hopfinger (1983) estimated an asymptotic velocity ratio (U_0) defined as the mean intercept from linear regressions of normalized (by linear propagation speed C_0) nose propagation speed versus both time and nose position. The value of U_0 is an estimate of the maximum nondimensional velocity in cases where the velocity decays with time. They reported a mean U_0 of 0.93 ± 0.14. In comparison, linear regression of the normalized nose propagation speeds after day three was made for each of the eight straight channel experiments reported here. Use of data after day three corresponded to Griffiths and Hopfinger's choice of data after the velocity maximum. The mean intercept was 0.91 ± 0.10. Mean intercept for only the experiments with decay of the nose propagation speed was

0.90 ± 0.13. Both values were in good agreement with the values reported by Griffiths and Hopfinger and with the slightly higher value (1.0 ± 0.1) of Stern, Whitehead and Hua (1982). The regression line plotted for experiment T6 in Figures 6a and 6b illustrates the location of U_0 and the growth mode of the experiments without detrainment.

Upstream Current Width Current width defined as distance from the wall to the two meter isopleth was measured in the channel at 60 and 80 *km* from the head of the channel and on the shelf at 20 and 40 *km* downstream of the channel mouth. This measure overestimated the velocity component e-folding scale by less than one kilometer in experiments T1 and T6 in the channel. On the shelf this measure appeared to underestimate the velocity component e-folding scale by about 30 percent for versions with detrainment and to overestimate the current width for those without detrainment by the same amount. Qualitative comparison of the interface contour plots and velocity plots suggest that this measure gave a consistent view, if not absolutely accurate in terms of e-folding scale, of the temporal behavior of current patterns in all versions and so was used in the statistical analyses that follow.

Figure 7 shows current width (normalized by Rossby radius) measured at both 60 and 80 *km* from the head of the channel plotted against time in inertial periods. The cases with large ε were all confined, with one exception, to less than 11 *km* ($2.5R_0$) from the wall while those with small ε tended to fill the majority of the channel width. The exception was the width at 60 *km* in experiment T, which

Figure 7. Current Width in Channel. Normalized current width (y/R_0) using 2 m isopleth in channel plotted versus time in inertial periods. Measured (a) 60 km and (b) 80 km from head of channel. Data grouped by ε (∇ =1.0×10^{-5}, $\bigcirc$ =5.0×10^{-6}, $\triangle$ <5.0×10^{-6}) and r_i (solid line = 0.035 $cm\ s^{-1}$, dotted line = 0.0035 $cm\ s^{-1}$, dashed line = 0.007 $cm\ s^{-1}$, and dash - dot line = 0.0 $cm\ s^{-1}$).

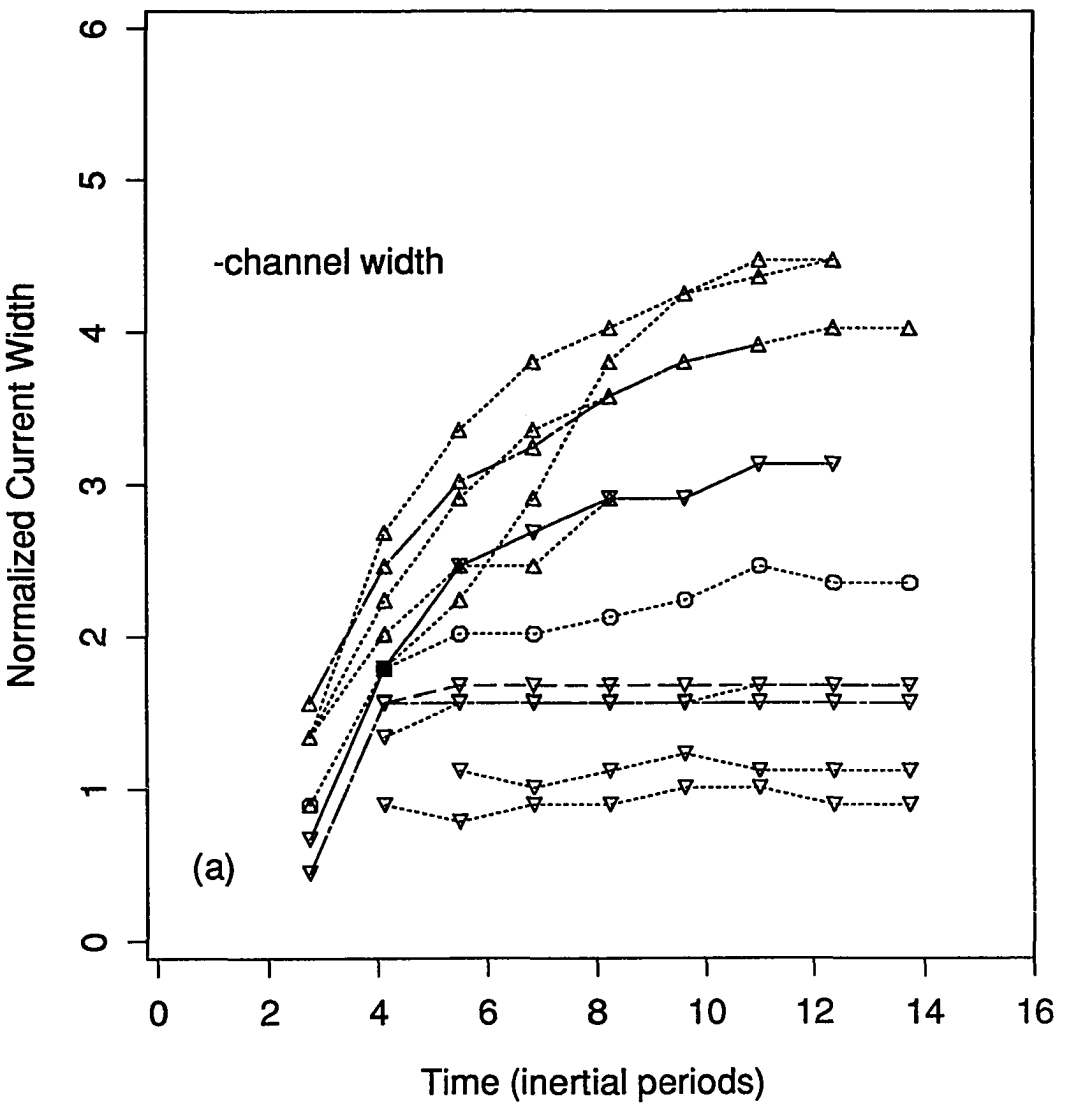

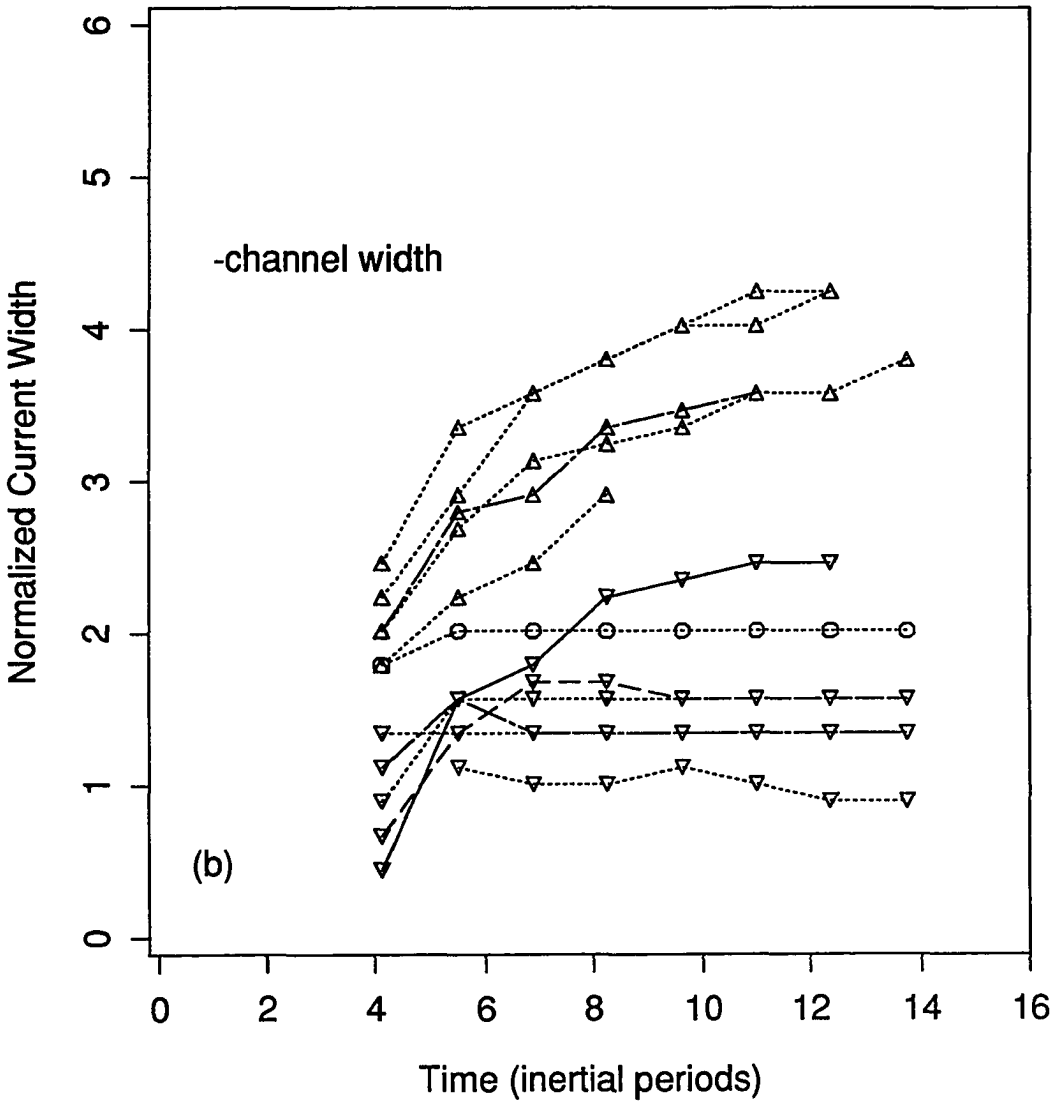

had the highest value for interfacial friction. Experiment T also had Rayleigh friction coefficient (r_i / h) and Newtonian cooling coefficient of the same magnitude, an important distinction which will be discussed later. Current profiles in the channel are shown in Figure 8; those with large ε (Figure 8a) were confined to a more jet like structure along the right hand wall and with higher velocity than the cases without detrainment. The cases with small ε (Figure 8b) had broad current profiles with highest currents toward the cepppppnter of the channel. Note that the velocity components in Figure 8 were scaled by inflow speed (27 $cm\ s^{-1}$ at steady state). Appearance of the interface contours and the velocity profiles were similar in being either broad or jetlike.

Measurements of current width 20 *km* along the shelf showed some evidence of southward propagation of the plume as evidenced by a strong correlation with time (correlation coefficients greater than 0.93) in experiments T3, T5, T6 and T7. Measurements at the 40 *km* mark are plotted in Figure 9. Current width at this mark was not well correlated with time except experiment T5 (correlation coefficient 0.960). Figure 10 shows the velocity profiles for experiments T1 and T6 at day ten and illustrates the differences between experiments with large and small ε. Mean current width at each mark was computed for each experiment and regressions performed versus both ε and interfacial friction. Current width at both marks was strongly correlated with ε (correlation coefficients of 0.959 at 20 *km* and 0.925 at 40 *km*) and poorly correlated with interfacial friction (correlation coefficients less than 0.04). It was interesting that the current in experiment T6 had

Figure 8. Current Profiles (u component) in Channel. Cross channel profile of u normalized by inflow velocity u_0 plotted against channel width normalized by Rossby radius (y/R_0) for (a) version T1 and (b) version T6. Measured on day ten at 60 km (□), 80 km (○) and 100 km (△) from channel head. Solid line identifies profile at 60 km. Arrow indicates width measured using 2 m isopleth at 60 km.

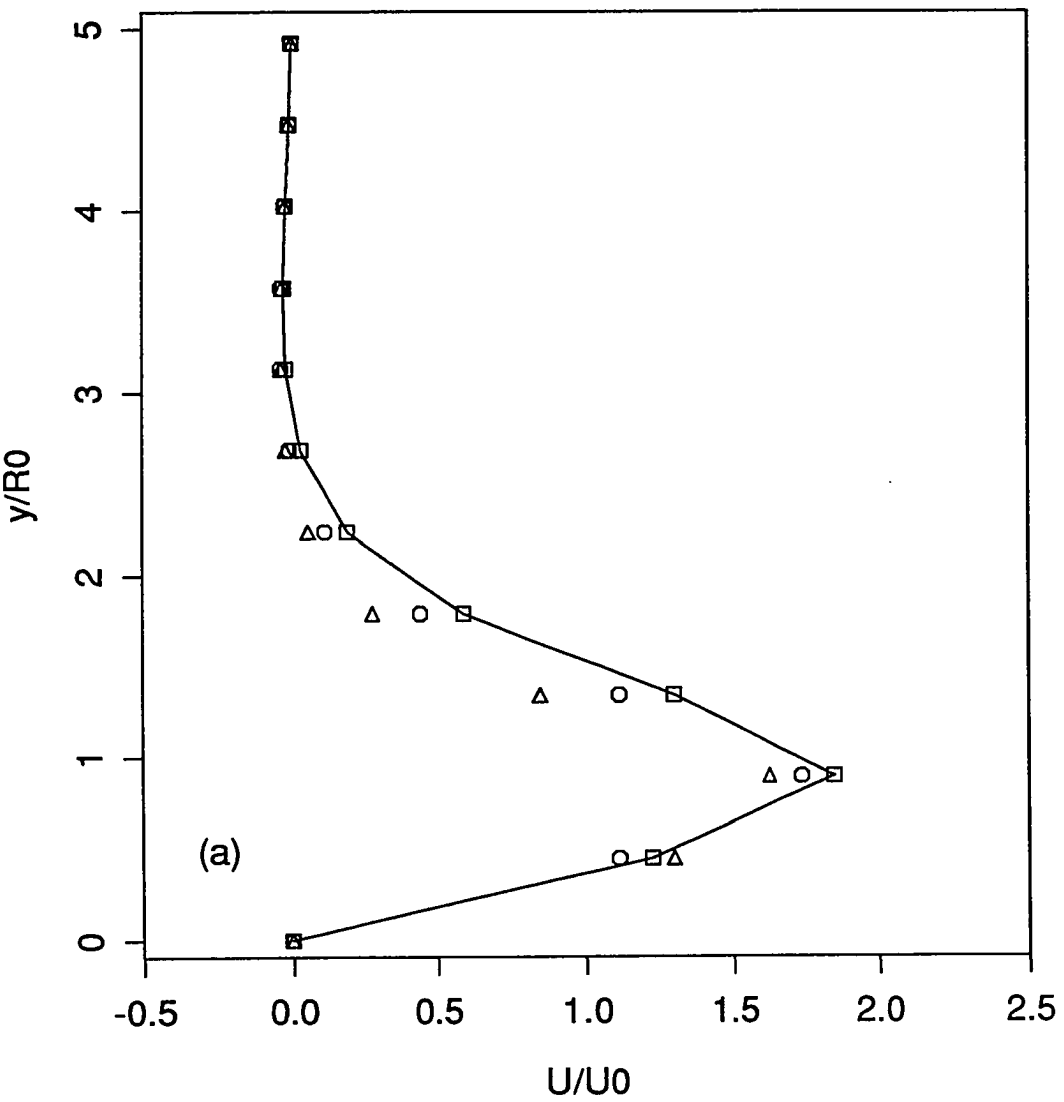

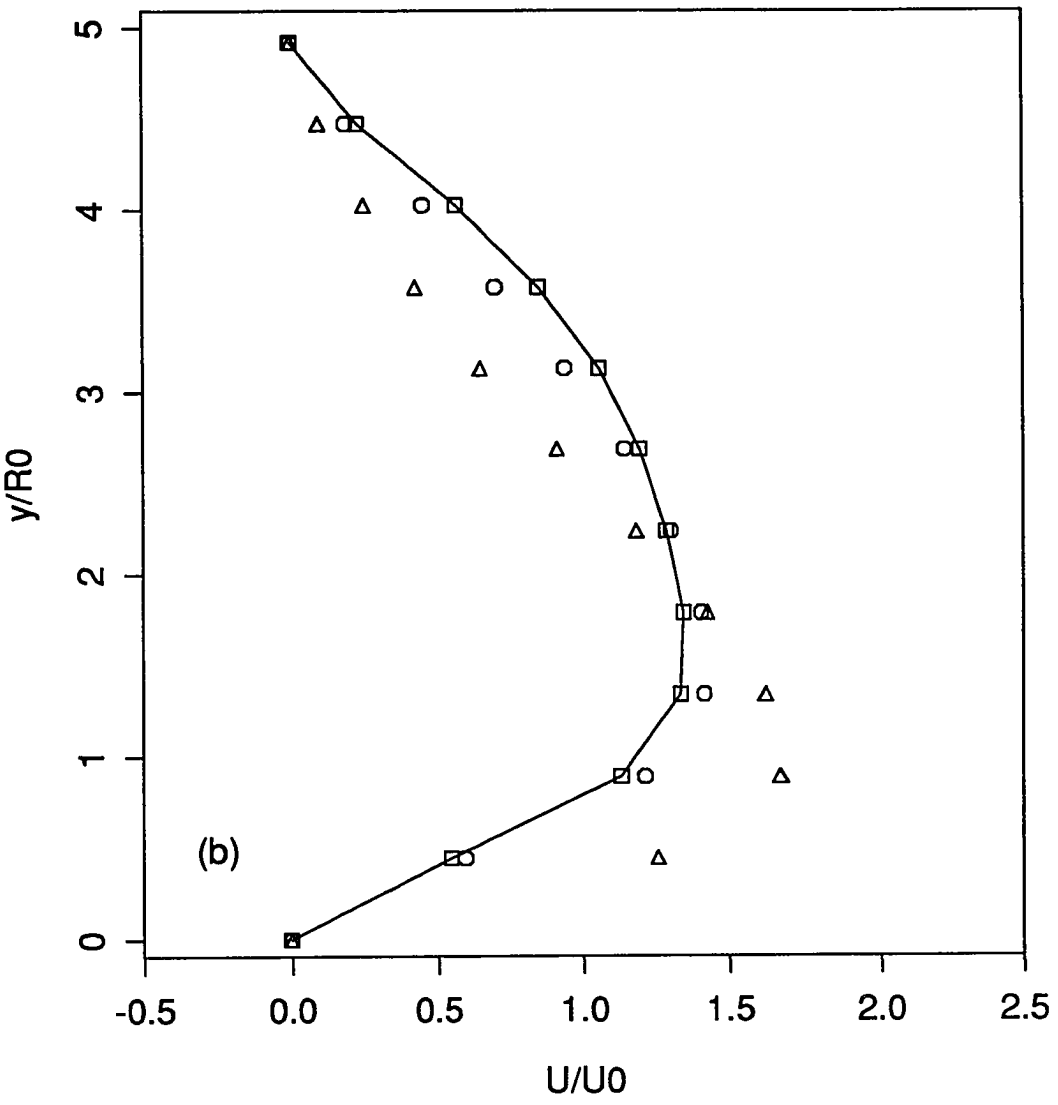

Figure 9. Current Width on Shelf. Normlized current width (x/R_0) versus time in inertial periods. Measured (a) 20 *km* and (b) 40 *km* from channel mouth. Data grouped by value of ε and r_i as in Figure 7.

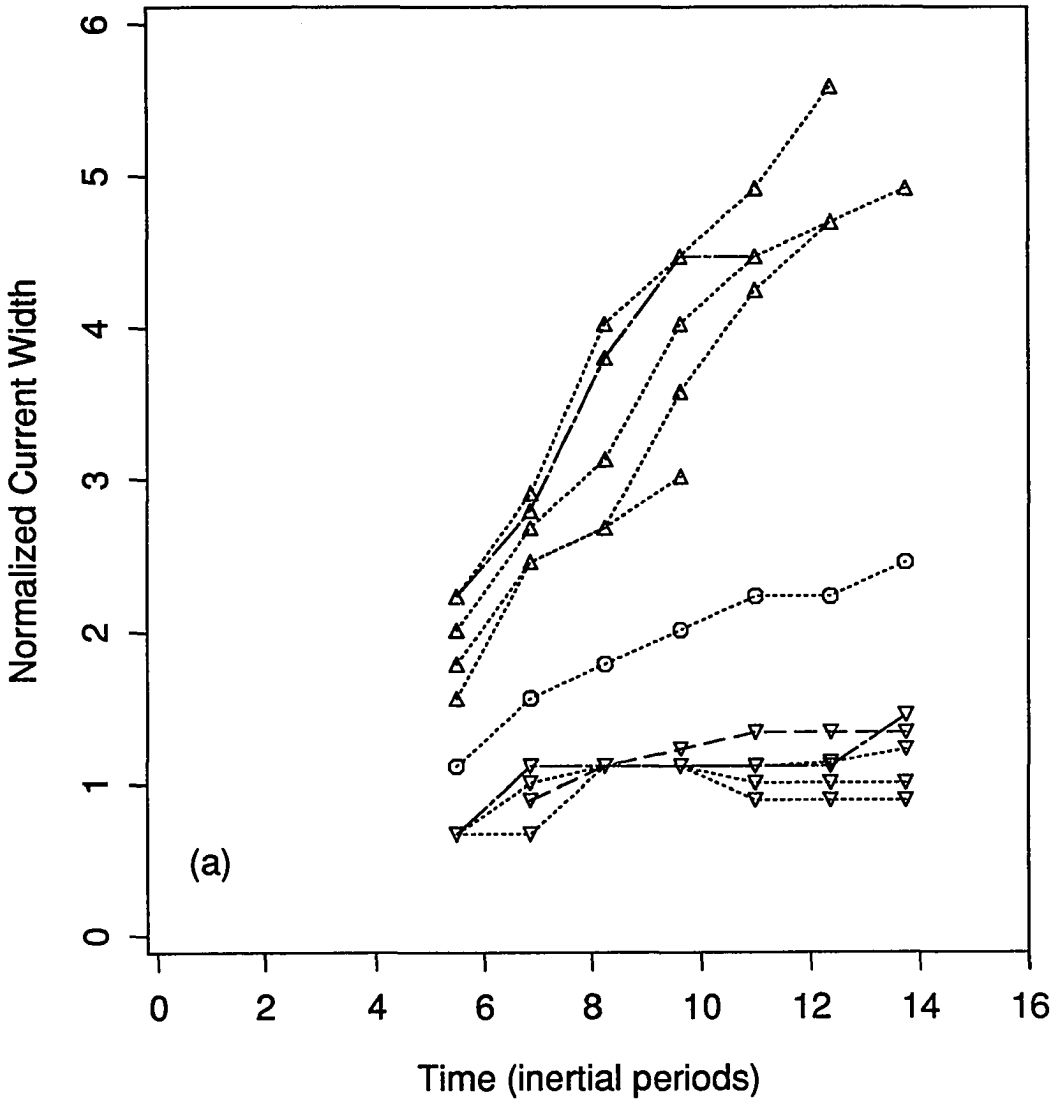

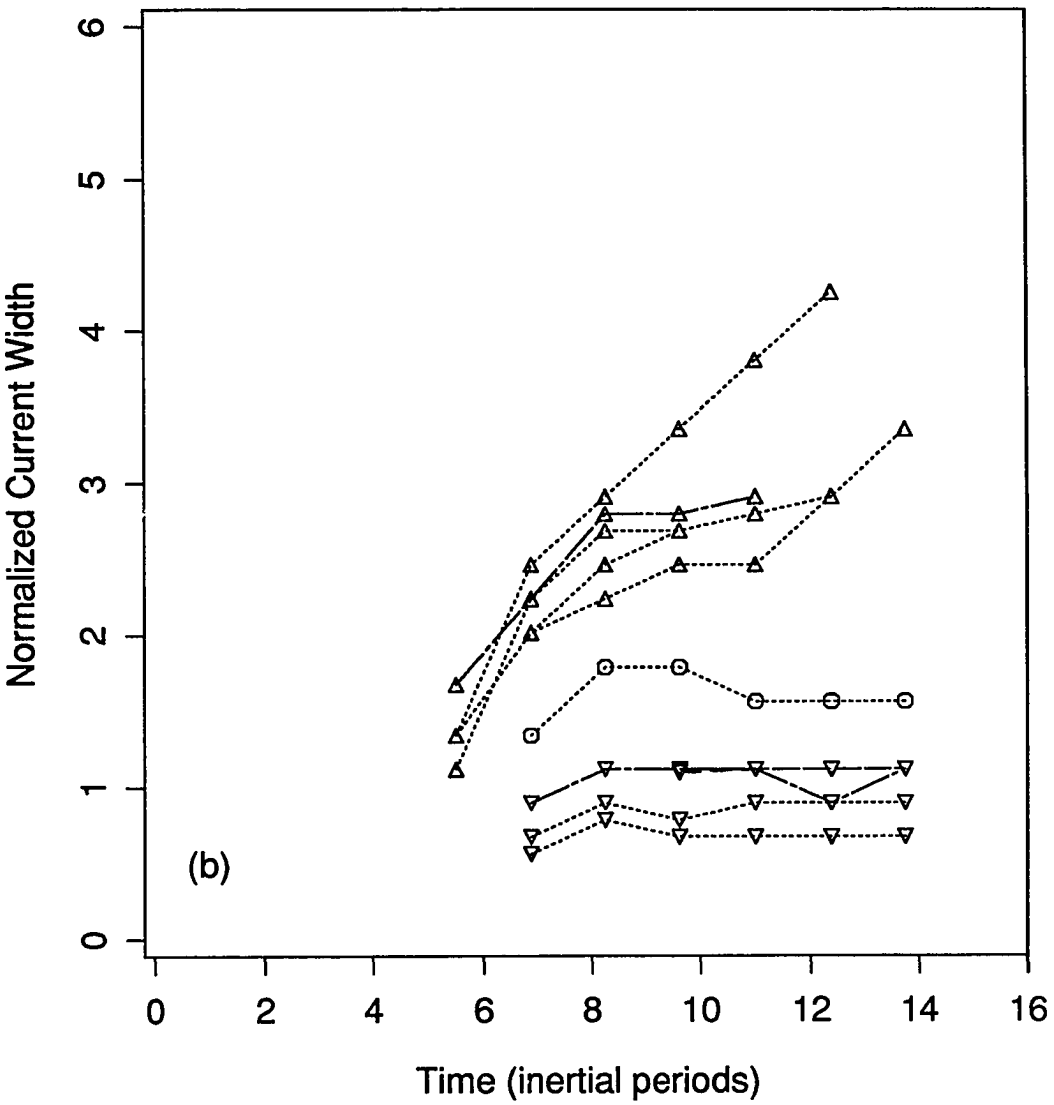

Figure 10. Current Profiles (v component) on Shelf. Cross shelf profile of v normalized by inflow velocity u_0 plotted against shelf width normalized by Rossby radius (x/R_0) for (a) version T1 and (b) version T6. Measured on day ten at channel mouth (△), 20 *km* (○), 40 *km* (□ and solid line) and 100 *km* (dashed line) from channel mouth.

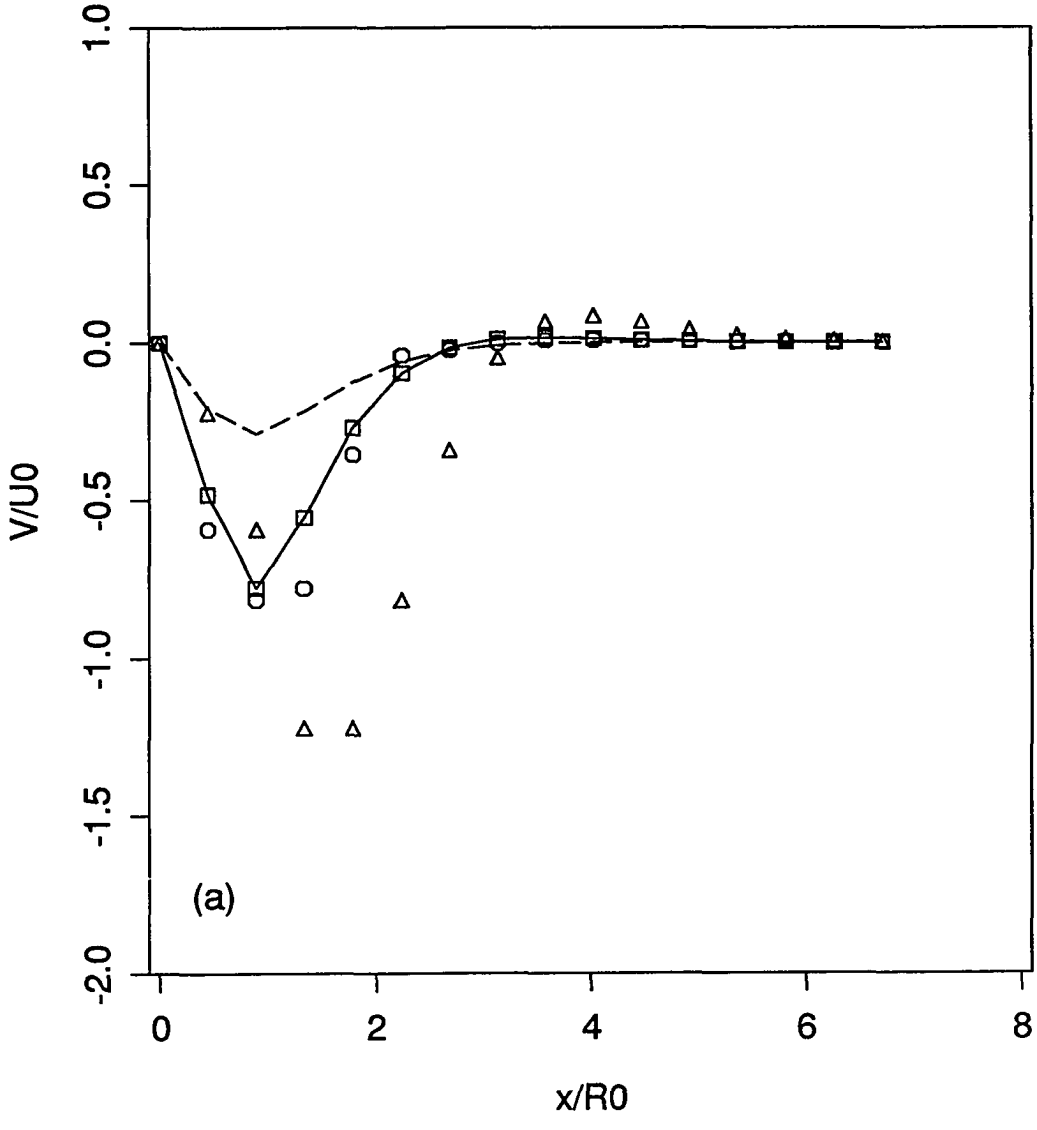

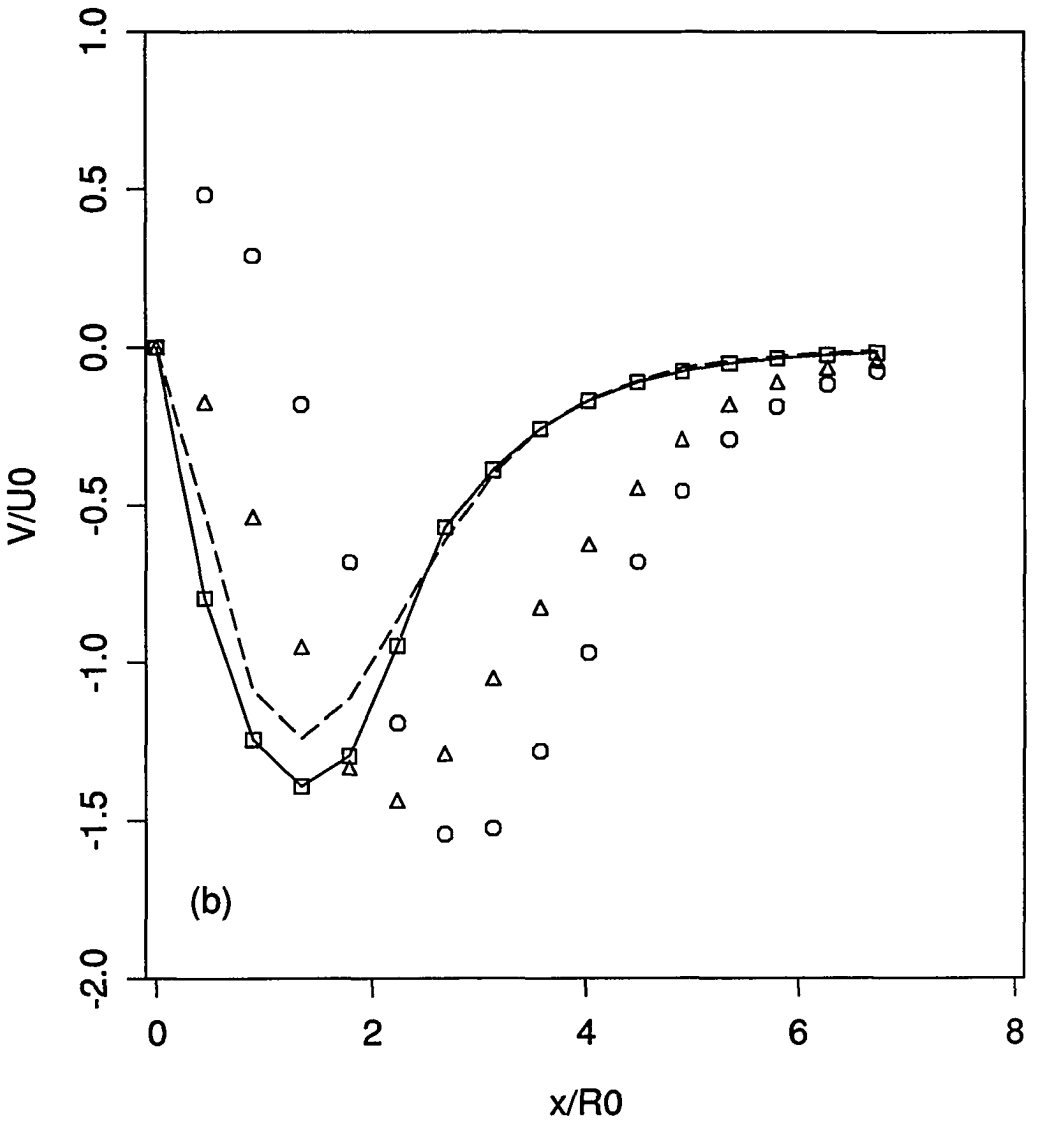

a more jetlike appearance on the shelf than in the channel. Maximum velocities in the coastal jet were virtually identical to those in the channel jet in the experiment without detrainment; however, in the experiment with detrainment the maximum velocity in the coastal jet was half that measured in the channel jet.

CHANNEL CONFIGURATION EFFECTS

Three channel orientations were considered. The straight channel (T series) was used to determine the effects of Newtonian cooling and interfacial friction as reported in the previous section. The "L" and "Γ" configurations were used in experiments with and without Newtonian cooling ($\varepsilon = 0.0$, $1.0\times10^{-5}\ s^{-1}$) and constant interfacial friction ($r_i = .0035\ cm\ s^{-1}$). Figures 2b and 2c show the "L" and "Γ" configuration dimensions, respectively, and the locations where current width measurements analogous to the straight channel case (shown in Figure 2a) were taken.

The principal physical differences between the configurations were the direction and location of corners looking downstream. Distance from the head of the channel to the shelf was a constant 100 *km* measured along the right hand wall. Corners where the channel turned left were classified as inside corners and those which turned right were classified as reentrant in the terminology of Cherniawsky and LeBlond (1986). The straight channel case had only one reentrant corner at 100 *km* from the channel head. The L channel had an inside corner at 70 *km* and a reentrant corner at 100 *km*. The Γ channel had a reentrant corner at 90 *km* and a second reentrant corner at 100 *km*.

In both L and Γ configurations the region of adjustment to geostrophy at the inflow appeared to be identical to the straight channel cases with comparable values of ε and interfacial friction. Distance travelled along the centerline of the channel (X_{CL}) was used as a measure of this similarity. Distance travelled was normalized by the centerline length (L_{CL}) of the appropriate channel. Mean normalized distance in cases without detrainment was $\overline{X}_{CL}/L_{CL} = 1.13 \pm 0.04$ after eight days. This distance (X_{CL}) was comparable to the mean penetration length ($\overline{L}_P$ /100 km) of 1.17 computed in the same experiments. In all cases without detrainment flow in the channel gave the appearance of being only weakly modified by rotation after an initial period of adjustment of about three days. Distance travelled along the right hand wall was compared with channel length along the right hand wall in a manner consistent with distance travelled along the centerline. Mean normalized distance along the right hand wall was 1.16 ± 0.03. In contrast, the cases with detrainment had a mean normalized centerline propagation distance of 0.22 ± 0.07. If the distance travelled were normalized by the centerline length to the first reentrant corner, the mean normalized propagation distance was 0.25 ± 0.04. Clearly the major differences were between versions with and without detrainment while differences in propagation due to configuration were more subtle.

Flow around the inside corner in case L was characterized by set down of the interface which represented available potential energy for conversion to kinetic energy. Cherniawsky and LeBlond (1986) described this phenomenon in terms of

centrifugal downwelling (or upwelling at a reentrant corner). Plot of nose position versus time indicated qualitatively that nose propagation speed was approximately equal to C_0 until the corner was reached after which it decreased slightly. This behavior is seen graphically in Figure 5. Linear regression of nose position versus time in the channel gave $C_c = 35.5\ km\ d^{-1}$ ($X_N = -5.3+35.5\ t$) and correlation coefficient of 0.989. Standard error of the propagation speed was $3.8\ km\ d^{-1}$. Computed propagation speed in the straight channel case with the same values for ε and interfacial friction ($1.0\times10^{-5}\ s^{-1}$ and $0.0035\ cm\ s^{-1}$, respectively) was $34.5\ km\ d^{-1}$ with a standard error of $0.866\ km\ d^{-1}$. The qualitative features noted were within the standard error of the data. A similar result for the Γ configuration was obtained where the propagation speed was $36.5\ km\ d^{-1}$ with standard error of $4.3\ km\ d^{-1}$. Propagation speed was 2.9% higher in the L channel and 5.8% higher in the Γ channel than the straight channel and with an order of magnitude greater variability in both cases. Some of the variability must have been due to the small sample size since only three data points were generally available in the channel. A separate short duration experiment in the straight channel allowed measuring nose propagation at six hour intervals. This data set gave $C_c = 34.3\ km\ d^{-1}$ with a standard error of $0.4\ km\ d^{-1}$. Most of the variability may thus be attributable to the presence of corners which generated Poincaré waves to be superimposed on the underlying Kelvin wave propagating in the channel, although it has not been possible to quantify this effect.

Once around the inside corner the current became wider than the current upstream of the bend. Figure 11 shows the interface contours and velocity vectors on day six for comparison with Figures 3g and 3h and Figures 4a and 4b. Figure 12, a plot of local Froude number ($F_{i,j} = U_{i,j} / (g^* h_{i,j})^{1/2}$) computed for day ten, shows a thin supercritical core ($F > 1$)) in the last 20 *km* of the channel. Such a supercritical core was not present in either the straight channel or Γ cases. Indication of supercritical flow was consistent with a locally widening flow, however it was interesting that the 'widening' occurred in a channel of constant width. The widening may have been caused by superposition of Poincaré waves generated at the inside corner.

Formation of the plume in the L channel case occurred at about day four as it did in the straight channel case shown in Figure 3c. The general features were similar except that the transition from channel to plume appeared to have an inflection in case L. By day ten the width of the plume was identical in both cases, however, in case L the plume was four meters deeper, had higher velocity (66.7 $cm\ s^{-1}$ vice 48.6 $cm\ s^{-1}$), and had a more complicated interface and velocity structure. The velocity structure was just beginning to show the anticyclonic gyre in the plume at day ten whereas it had appeared in the straight channel case within two days after the intrusion rounded the corner. Once this gyre developed it remained a feature of the plume. The interface rose as the intrusion approached the reentrant corner, deepened after rounding the corner, rose again , fell to its lowest depth along the wall and then rose again sharply as the flow transitioned from the

Figure 11. Interface Contours and Currents. Model version L1 with r_i=0.0035 $cm\ s^{-1}$ and $\varepsilon = 1.0\times10^{-5}\ s^{-1}$. (a) Interface depth ($h-h_0$) contours at 200 cm intervals and (b) current vectors on day six.

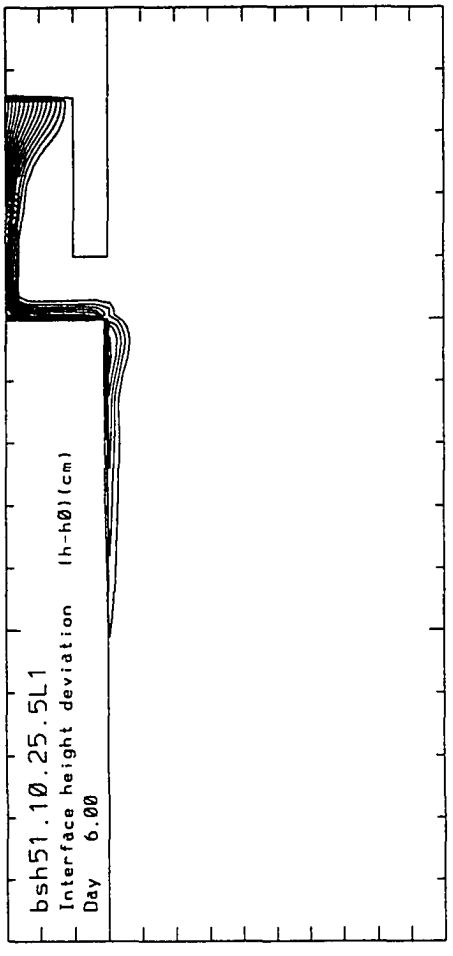

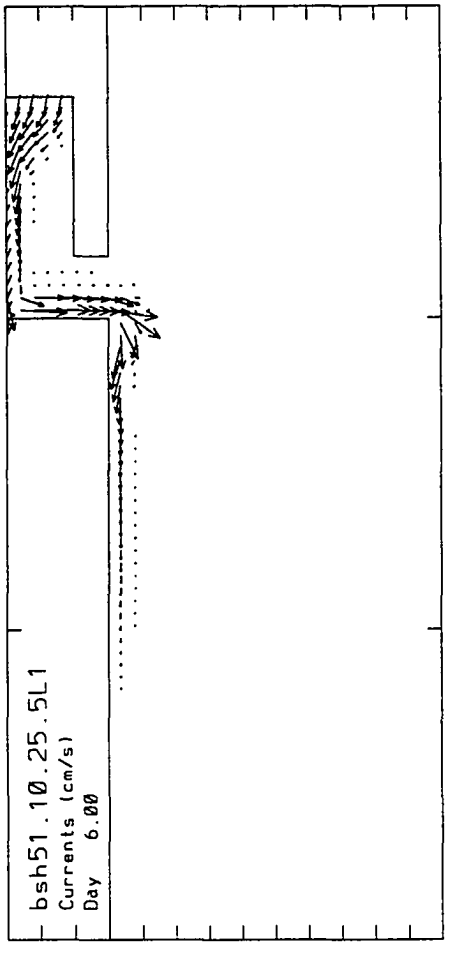

Figure 12. Local Froude Number. Model version L1. Data from day ten in 50 *km* square around channel mouth. Contour intervals 0.01, 0.1, 0.5, 1.0 and 1.4. Dotted line indicates two meter isopleth.

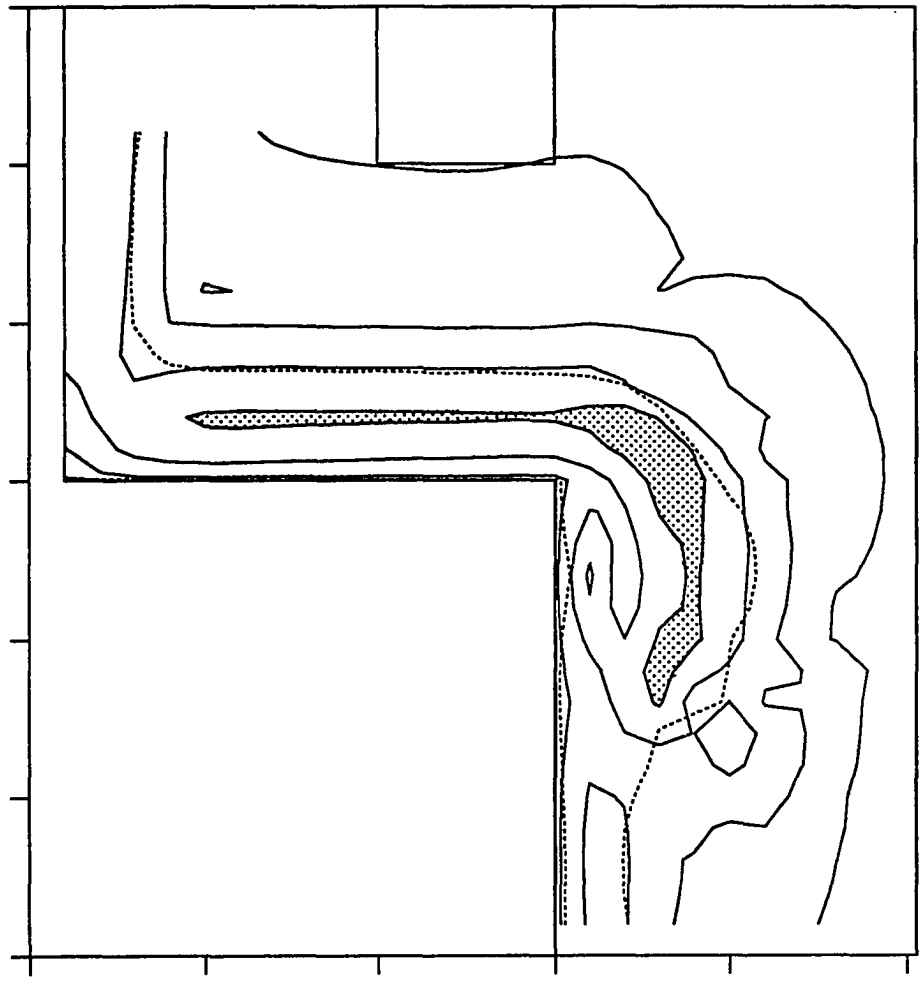

plume structure to a coastal jet. The small cyclonic gyre reported on the outer rim of the plume in the straight channel case was only weakly evident in case L. A broad band of supercritical flow characterized the outer edge of the plume from 12 to five o'clock with a radius of approximately six kilometers (or approx $1.4\,R_0$) with the center located at the wall in the region where the interface was rising. Supercritical flow was also indicated at the center of the roughly elliptical arc.

Formation of the plume in case Γ took place at the first reentrant corner which placed the plume inside the channel mouth. This plume developed earlier and faster and was approximately three kilometers wider at day ten. Figure 13 shows the interface contours and velocity vectors for this experiment on day six for comparison with Figures 3, 4 and 11. Initially a widening of the coastal current occurred which looked like a second plume. This feature lasted only a day or so and did not separate from the wall. Velocities in the plume were the highest ($103\ cm\ s^{-1}$) noted in any of the experiments. Because of the location of the plume inside the channel mouth a complex circulation pattern developed in the upstream portion of the channel. As the channel jet impinged on the opposite wall 110 *km* downstream from the head, a cyclonic eddy developed which dominated the left corner of the channel and rejoined the plume. The core of supercritical flow in the channel jet in case L was not present in this case. The supercritical flow arc in the plume had the same radius ($\approx 1.4\,R_0$) as the two previous examples. The highest Froude number in Figure 14 was three times higher than case L and was found in a small center where the cyclonic eddy rejoined the plume. Supercritical flow here

Figure 13. Interface Contours and Currents. Model version $\Gamma 1$ with r_i=0.0035 $cm\ s^{-1}$ and $\varepsilon = 1.0\times10^{-5}\ s^{-1}$. (a) Interface depth $(h-h_0)$ contours at 200 cm intervals and (b) current vectors on day six.

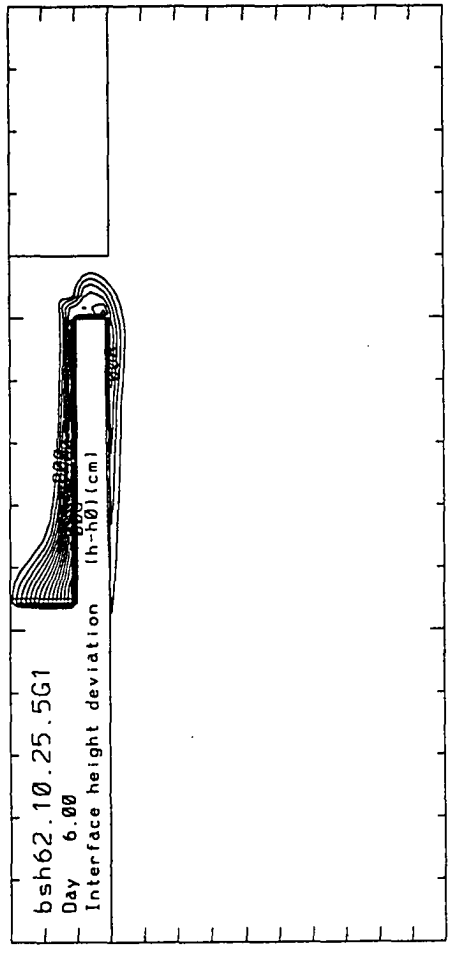

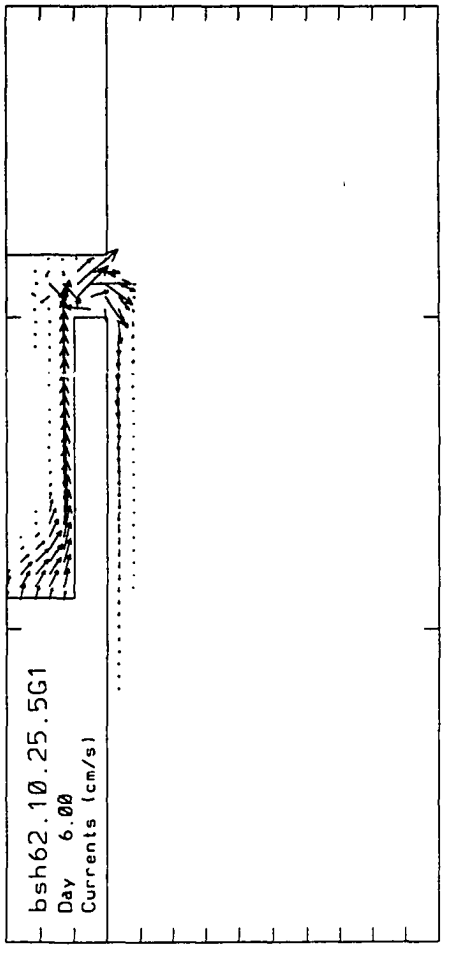

Figure 14. Local Froude Number. Model version Γ1. Data from day ten in 50 *km* square around channel mouth. Contour intervals 0.01, 0.1, 0.5, 1.0, 3.0 and 6.0. Dotted line indicates two meter isopleth.

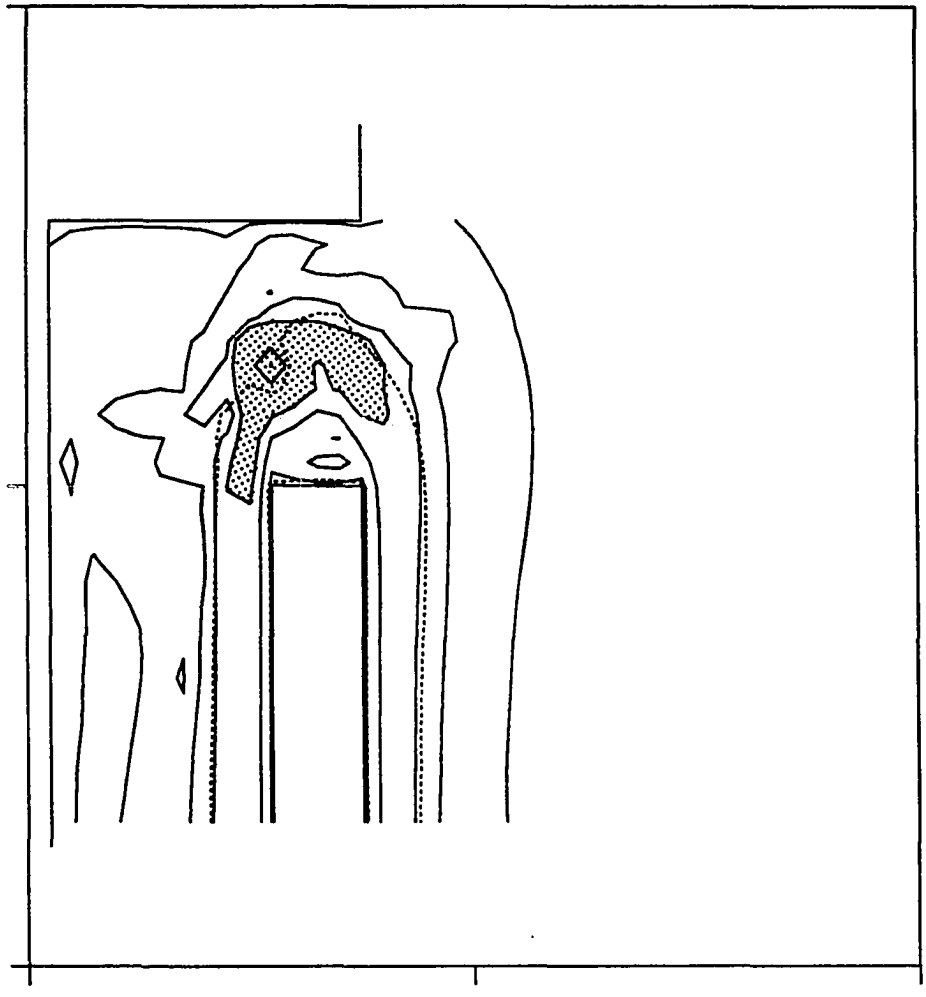

was in a more circular pattern and did not have supercritical region at the center of the arc as in case L.

Propagation speed of the coastal jet decreased as in the straight channel case as shown in Figure 5. Other significant features of the coastal jet were essentially identical to those in the straight channel case, except velocity relative to the inflow velocity u_0. Width of the jet showed no dependence on time and was constant over the 20 *km* distance between marks. Figure 15 shows the velocity profiles measured 20 *km* and 40 *km* downstream from the channel mouth. Flow in the jet was subcritical. Contrary to Cherniawsky and LeBlond's (1986) prediction that a flow which separated from the wall would remain separated, the coastal jet in this and every other case reattached to the right hand wall approximately 20 *km* downstream from the channel mouth except case Γ. Case Γ had the flow reattached at the channel mouth as it rounded the second reentrant corner.

Penetration length (L_p) and decay time were computed for both channel and shelf data as described in a previous section. There it was reported that channel penetration length and decay time for both regimes (shelf and channel) correlated with ε. Neither penetration length nor decay time were correlated with interfacial friction. Again, neither measure correlated with interfacial friction. The correlation coefficients relative to Newtonian cooling were lower when the data from these experiments was included. Here these measures were regressed against channel length, channel width, maximum depth at the head of the channel and maximum velocity. Penetration length was proportional to and well correlated with channel

Figure 15. Velocity Profile Across Shelf. Profiles of v-component normalized by inflow velocity u_0 plotted versus cross shelf distance normalized by Rossby radius (x/R_0). Profiles are for T1 (dotted line), L1 (dash line), Γ1 (dash dot line) and T6 (solid line) at (a) 20 *km* and (b) 40 *km*.

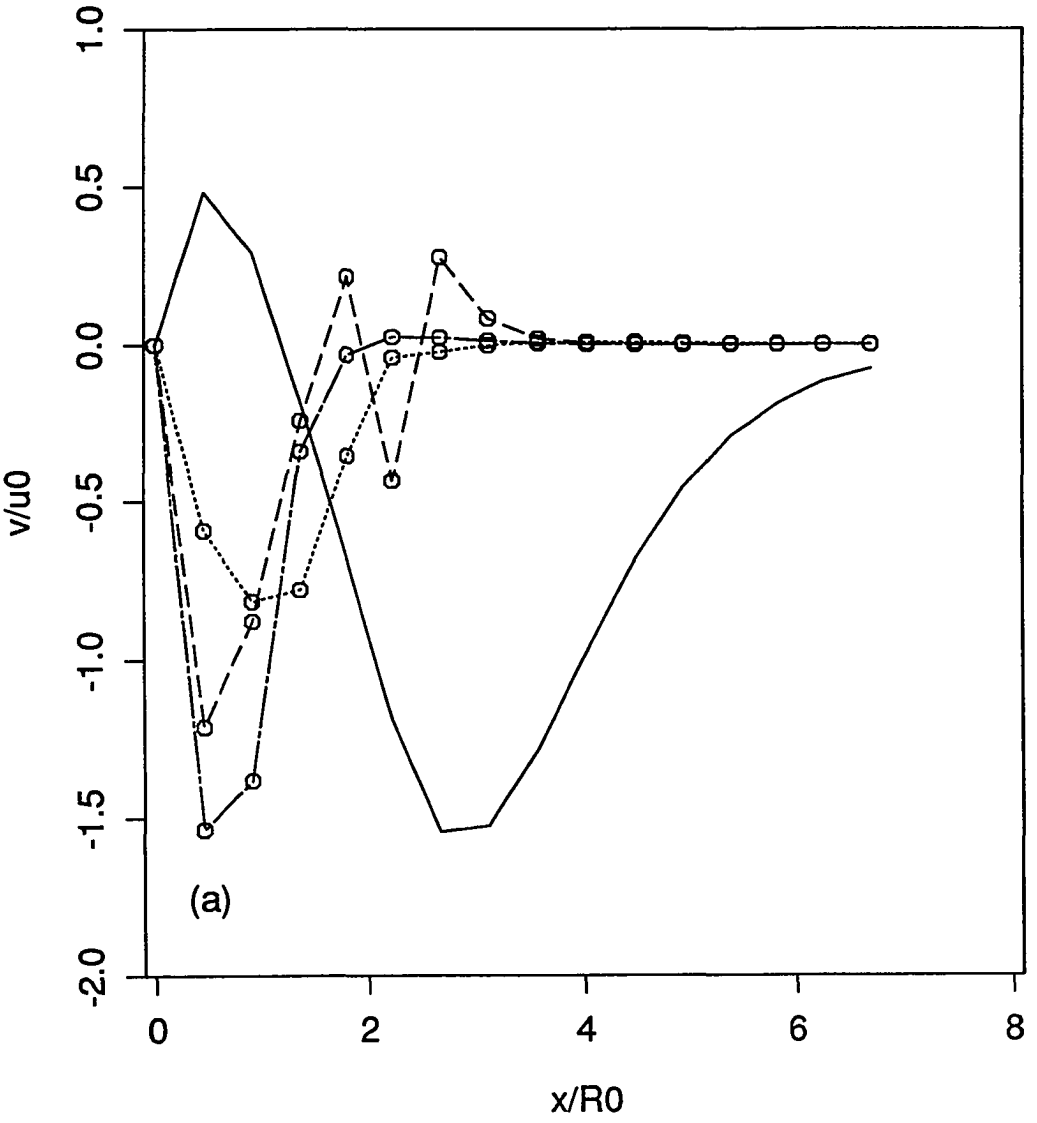

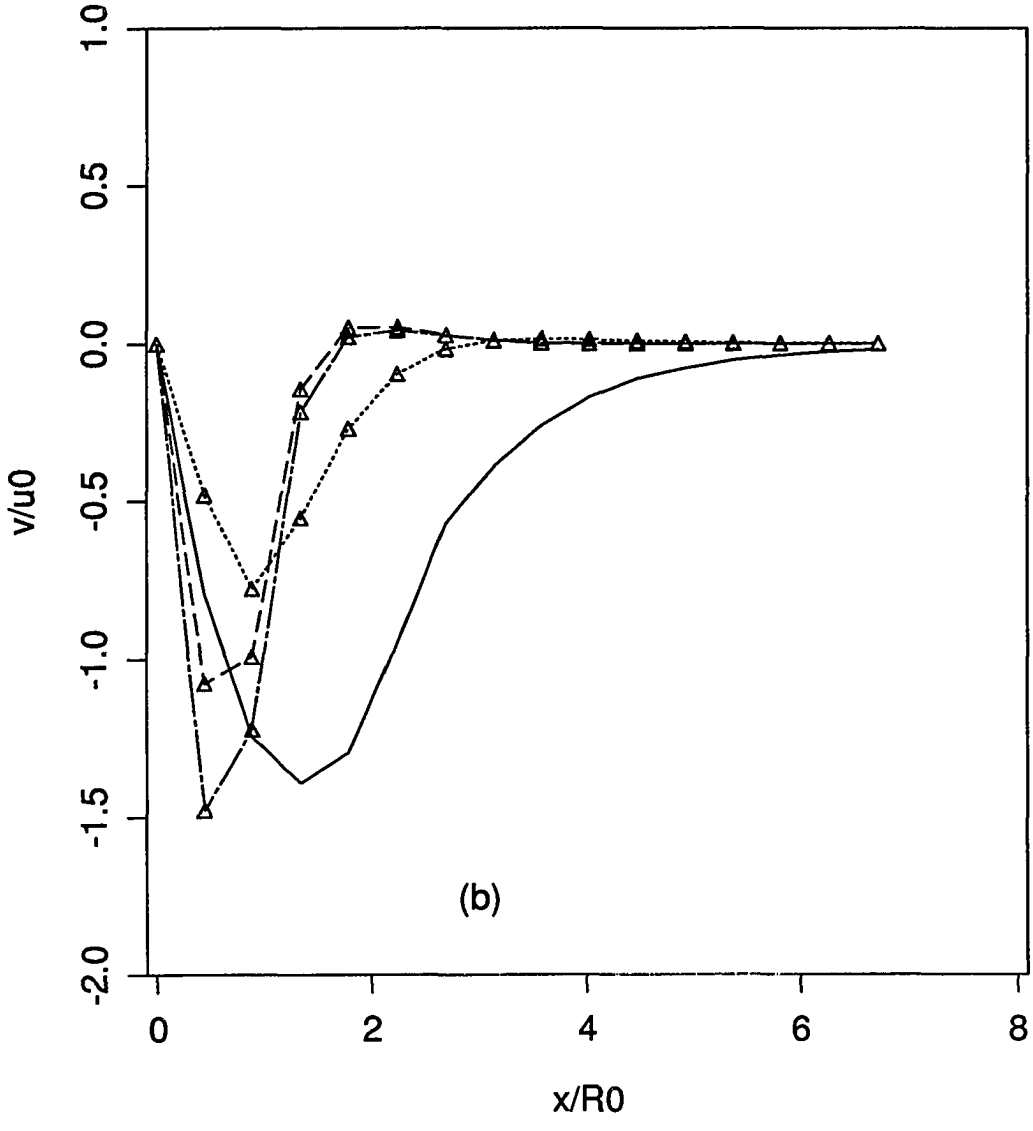

length (correlation coefficient 0.918) when Newtonian cooling was allowed. It must be noted that only one of the data points represented a shorter channel (80 *km* vice 100 *km*), yet the data strongly suggested that decay of the current in the channel was due to the presence of the mouth.

WIND EFFECTS

Wind stress of constant magnitude (0.5 *dynes* cm^{-2}) and direction was applied at day ten and left on for three days. Wind stress direction, in the oceanographic sense, was either northward, southward, eastward or westward. The dominant wind effect was the production of upwelling or downwelling along the coastal boundary. Northward ($\tau^y > 0$) winds produced upwelling at the coast boundary and along the right (left) hand channel wall in case L (Γ). Southward ($\tau^y < 0$) winds produced downwelling at the coastal boundary and along the right (left) hand channel wall in case L (Γ). Eastward ($\tau^x > 0$) and westward ($\tau^x < 0$) winds produced upwelling or downwelling in the east-west portion of the channel. The plume remained a prominent circulation feature attached to the coast in every case.

Northward wind caused upwelling which destroyed the cross shelf pressure gradient and the jet retreated along the coast toward its origin (nominally 20 *km* downstream from the mouth) in the plume. In the straight channel case the jet retreated 67 *km* in one day, then disappeared within the next day. It did not reappear. In case L it retreated rapidly to within 30 *km* of the plume ($C \approx 121.0$ *km* d^{-1}) in one day, continued another 20 *km* toward the plume for another day and then propagated back downstream 27 *km* when the wind stopped. Case Γ retreated 101 *km* in the first day, a rate roughly midway between the other two cases, then

was nearly stationary for half a day, advanced for a day and finally retreated. Figure 16 shows changes in coastal jet nose position and plume width versus time for northward and southward winds. The origin in each case is the nose position and plume width at day ten. Upwelling favorable wind had little effect on the plume width except that there was more variability in case Γ than in the other two. Northward wind moved the plume slightly offshore, the expected direction for Ekman transport. In case Γ, however, the plume was inside the channel mouth and possibly more susceptible to the effects of setdown than to Ekman transport.

The effects of downwelling favorable southward wind on nose position and plume width are also shown in Figure 16. In each case the jet moved out of the model domain within about one day after the wind was turned on. Determination of the phase speed was not possible except in the straight channel case where it was twice the linear propagation speed. Effects on plume width were again small except in case Γ where the plume expanded to fill the channel mouth.

Experiments with onshore (westward, $\tau^x < 0$) and offshore (eastward, $\tau^x > 0$) winds had less dramatic effects on the coastal jet and the plume than their alongshore counterparts. Maximum excursion of the nose was 43 *km* in 12 hours, a retreat of the nose in case L followed by propagation downstream at about 18 $km\ d^{-1}$. Westward wind in the straight channel case caused the coastal jet to propagate downstream but also, because of upwelling in the channel, slowed the outflow from the channel. A combination of reduced flow into the plume and setdown at the coast caused the jet to separate from the plume for about one day,

Figure 16. Effects of Northward and Southward Winds. Effects of 0.5 *dynes/cm*^{2} northward (open symbols) and southward (solid symbols) wind stress on (a) nose position and (b) plume width. Data cover three days for versions T1 (□), L1 (○) and Γ1 (△). Data were plotted relative to nose position and plume width on day ten, when the wind was turned on.

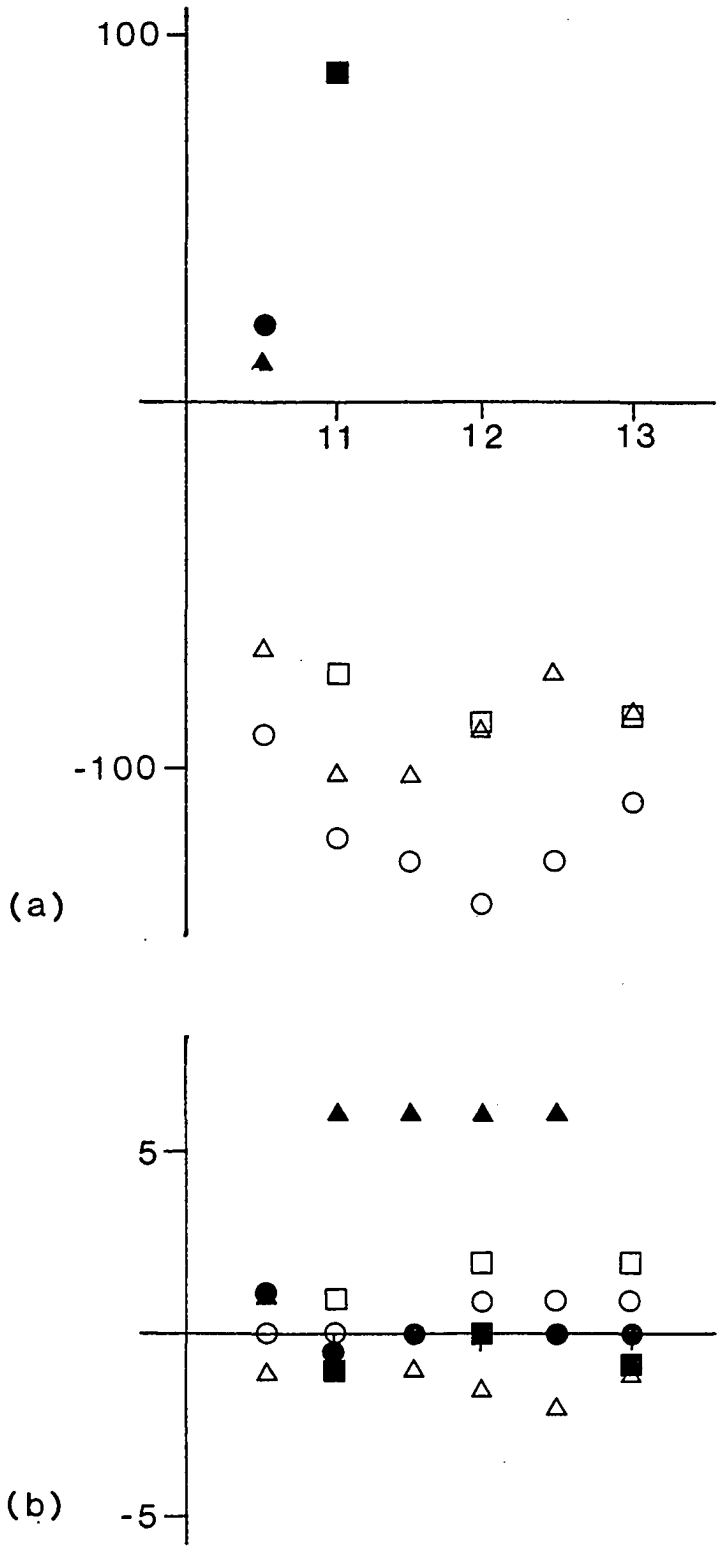

after which the channel flow increased, the plume widened and a second jet propagated downstream and overtook the first jet.

CHAPTER 4

SUMMARY AND CONCLUSIONS

This study has shown that detrainment processes modelled by Newtonian cooling were responsible for deceleration and eventual stagnation of a density intrusion along a continental shelf. It has been shown that when vertical mixing of momentum, in the form of Rayleigh friction ($r^* = r_i/h$), had the same time scale as mixing of density (Newtonian cooling) then mixing of momentum dominated the equations for Kelvin and Poincaré waves, the only wave solutions possible in a rotating channel. Examination of the linear equations for a single layer system showed that when friction dominates, the phase speed for both waves was the standard inviscid form with friction accounted for by an exponential time decay term. When both detrainment and interfacial friction were to be accounted for the dispersion relation for both waves suggested that phase speed was combination of the inviscid form with an added arbitrary function of both detrainment and interfacial friction and the exponential decay term involved both wave number and detrainment and interfacial friction. A more detailed discussion of the role of interfacial friction and Newtonian cooling in the wave solutions may be found in Appendix B.

In the experiments without detrainment interfacial friction caused the phase speed to decrease by about 3.5 percent. Inclusion of the nonlinear terms was shown experimentally to increase the phase speed by about the same amount. The

experiments with negligible Newtonian cooling coefficient showed constant phase speed everywhere, which suggested that interfacial friction balanced the nonlinear terms, at least in the channel jet and coastal jet. For reasonable values of detrainment and interfacial friction, i.e., those with which this model qualitatively duplicated previous results of three-dimensional numerical models and laboratory models, the propagation speed was constant in the channel and decayed on the shelf. The ratio of phase speed in the channel to phase speed on the shelf approximated that found by Chao and Boicourt (1986) in a three-dimensional model. Phase speed in the channel was less than linear wave phase speed. A key dynamical question was why detrainment seemed to affect flow on the shelf but not in the channel.

In theory the dynamic fields are established by the passage of non-dispersive Kelvin waves and a wake of Poincarè waves. Poincaré waves are all at frequencies higher than the inertial frequency and just begin to propagate energy at a critical frequency, here $1.222\,f$ related to the channel width. These lower frequencies also contain mostly kinetic energy (very high kinetic energy to potential energy ratios.) The Kelvin wave on the other hand has kinetic energy to potential energy ratio of unity. These characteristics suggest that energy accumulates in the inflow bulge and later in the plume as a result of the highly dispersive quality of the lowest frequency Poincaré waves. Energy is lost by the radiation of higher frequency Poincaré waves. In the channel with constant inflow the waves can only propagate downstream. In the absence of detrainment the waves propagate downstream in

such a way that the Poincaré waves eventually spread out to fill the channel with both potential and kinetic energy. In this series of experiments this type of behavior was found in all cases where the Newtonian cooling coefficient was the same order of magnitude as Rayleigh friction. Detrainment, however, dissipates the potential energy in the higher frequency, propagating Poincaré waves and the flow is confined within a small distance ($1.5\,R_0$) of the right hand wall after the passage of the waves. At the open end of the channel a set of cylindrical Poincaré waves are generated, again in such a way that some energy accumulates in the bulge, some propagates along the right hand coast in the form of a Kelvin wave and the remainder radiates away in all directions in the form of the higher frequency Poincaré waves. Some small amount of this energy may radiate back into the channel, either directly or through interaction with the opposite corner, in such a way as to block the channel. Such behavior is suggested at least qualitatively in Figure 17 which shows the interface contours in the vicinity of the channel mouth for experiment T1 such that even the small amplitude variations are shown.

Based on these experiments it is possible to describe the flow in terms of the Rossby adjustment problem in two domains; the channel and the shelf. The entire flow field can be partitioned into five regions with important differences in the dynamics. The differences between channel configurations can be described also in terms of Kelvin and Poincaré wave propagation and interactions with corners. The five regions are;

Figure 17. Interface Contours. Model version T1. Same as Figure 3 except interface height less than ten centimeters were not smoothed out. Elevations outside the plume in vicinity of the mouth were approximately ten centimeters above h_0. Elevations beyond approximately $20km$ from mouth decreased to $O(10^{-3})$ or smaller.

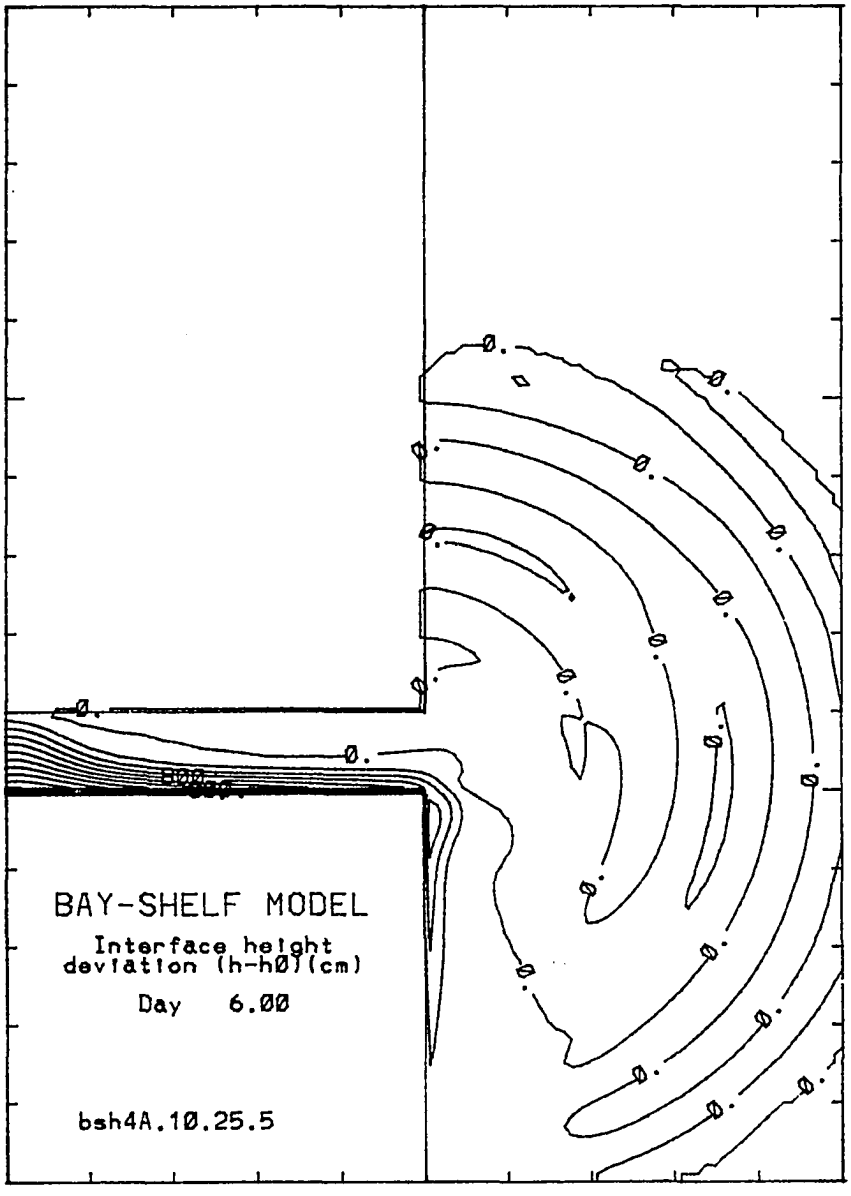

- Inflow bulge,
- channel jet,
- plume,
- coastal jet and
- nose.

The nose region in this model was essentially featureless as might be expected in a two-dimensional model and is not discussed in any further detail. The inflow region was weakly nonlinear only in the area less than one Rossby radius from the source of less dense water. Coriolis forces dominated the bulge as the flow adjusted to geostrophy. The bulge propagated very slowly downstream and appeared to stop in the presence of detrainment but propagated past the channel mouth when detrainment was not included in the model. However both reached an equilibrium position after about six days consistent with the rate of change of the inflow. This case differs from the rotating tank experiments, the theoretical work of Gill (1977) and the numerical study of Wang (1985) in that the constant inflow precludes reverse flow along the left hand wall or the formation of an anticyclonic gyre in the lock. Such a gyre is believed to be an end wall effect. Energy was carried away from the inflow bulge by currents set up after the passage of the Kelvin wave and the wake of Poincaré waves.

Geostrophic flow developed along the right hand wall after the passage of the waves. In experiments without detrainment the geostrophic flow was modified by the propagation of higher frequency Poincaré waves, which, it is theorized, caused the current to widen. The current was maintained by the constant supply of low density water from the bulge so the geostrophic equilibrium shape of the interface

set up by passage of the waves was maintained by mutual adjustment. Examination of the Bernoulli function showed the mechanical energy of the system to be nearly constant and concentrated along the right hand wall until the mouth of the channel was reached. Flow in the channel remained subcritical. When the channel had an inside corner the addition of energy from cylindrical Poincaré waves propagating down channel caused the flow to widening of the current to the addition of terms of order of the Rossby number. Here the ratio of kinetic energy to potential energy jumped 20 percent. This effect was masked in the experiments with negligible detrainment which remained subcritical everywhere.

Once at the channel mouth the flows with detrainment became supercritical in an arc around the outer edge of the flow and developed a strong and persistent anticyclonic gyre to the right of the mouth. One consequence of the locally supercritical flow was that signal propagation in the form of waves could not propagate through the region. The channel was thus effectively blocked at the mouth. Whatever energy might be carried by Poincaré waves along the left half of the channel could not propagate downstream. Supercritical flow indicated unstable flow where vertical mixing was an important part of the dynamics. The supercritical region of the flow was dominated by Coriolis force but the nonlinear terms had their greatest magnitude here as well. The region of transition back to subcritical flow was highly nonlinear, with the nonlinear terms one to two times larger than the inertial terms. The arc of supercritical flow was also the locus of maximum kinetic energy in the system and of maximum gradient in potential vorticity.

While the channel jets were quite different in experiments with and without detrainment, the coastal jets were qualitatively similar in cross section. The experiments with negligible detrainment had virtually identical velocity in the channel and on the shelf which suggested that energy was being propagated downstream with minimal dissipation. The experiments with detrainment clearly showed that energy was being lost from the system on the shelf since the jet here had velocities less than half those in the channel jet. Velocity in the coastal jet with detrainment decayed downstream whereas the velocity structure had been almost constant along the channel length.

Wind effects on the coastal jet were qualitatively similar to those reported by Chao (1987). Wind had almost no effect on the plume, however, in marked contrast to Chao (1987). Here the plume was a strongly persistent feature which maintained its shape and position. The Ekman depth for this series of experiments was approximately 2.5 m, which was not well resolved in the model. In related experiments without wind where the inflow was turned off after day ten, the plume was the last feature of the flow to disappear.

Unresolved Issues In general the model has been robust, however some stability problems have been encountered in relation to the open boundary when the flow dynamics admitted the possibility of upstream propagating disturbances. Stability problems have also occurred near the inflow after short time periods in linear versions of the model. Apparent instabilities on the outer edge of the flow near the source developed after ten model days reminiscent of instabilities in the same

relative location reported by Griffiths and Hopfinger (1983). There appeared to be some susceptibility to small perturbations in inflow velocity after day ten. None of these phenomena have been investigated in detail in this study. This problem should be a fruitful one for future work, in particular in regard to differentiating numerical instabilities from those which have physical meaning.

The form of the dispersion relations for Kelvin and Poincaré waves worked out in Appendix B is not complete. It may only be possible to achieve a numerical solution for these relations, but this has not been done. The experimental evidence at least suggests that the approach is correct.

REFERENCES

Beardsley, R.C. and J.R. Hart, 1978, A simple theoretical model for the flow of an estuary onto a continental shelf, *J. Geophys. Res., 83,* 873-883.

Bennett, J.R., 1973, A theory of large amplitude Kelvin waves, *J. Phys. Oceanogr., 3,* 57-60.

Boicourt, W.C., 1973, The Circulation of Water on the Continental Shelf from Chesapeake Bay to Cape Hatteras, PhD Thesis, The Johns Hopkins University, Baltimore, MD, 183pp.

Buchwald, V.T., 1968, The diffraction of Kelvin waves at a corner, *J. Fluid Mech., 31,* 193-205.

_____, 1971, The diffraction of tides by a narrow channel, *J. Fluid Mech., 46,* 501-511.

Chao, S.-Y. and W.C. Boicourt, 1986, Onset of estuarine plumes, *J. Phys. Oceanogr., 16,* 2137-2149.

_____, 1987, Wind driven motion near inner shelf fronts, *J. Geophys. Res., 92,* 3849-3860.

Chapman, D.C., 1985, Numerical treatment of cross-shelf open boundaries in a coastal ocean model, *J. Phys. Oceanogr., 15,* 1060-1075.

Cherniawsky, J. and P.H. LeBlond, 1986, Rotating flows along indented coastlines, *J. Fluid Mech., 169,* 379-407.

Csanady, G.T., 1984, The influence of wind stress and river runoff on a shelf-sea front, *J. Phys. Oceanogr., 14,* 1383-1392.

Garvine, R.W., 1982, A steady state model for buoyant surface plume hydrodynamics in coastal waters, *Tellus, 34,* 293-306.

_____, 1987, Estuary plumes and fronts in shelf waters: A layer model, *J. Phys. Oceanogr., 16,* submitted.

Gibbs, R.J., 1970, Circulation in the Amazon River estuary and adjacent Atlantic Ocean, *J. Mar. Res., 28,* 113-123.

Gill, A.E., 1976, Adjustment under gravity in a rotating channel, *J. Fluid Mech., 77,* 603-621.

_____, 1982, **Atmosphere-Ocean Dynamics**, Academic Press, Orlando, FL, pp 662.

Holland, W.R. and L.B. Lin, 1975, On the generation of mesoscale eddies and their contribution to the oceanic general circulation. I. A preliminary numerical experiment, *J. Phys. Oceanogr., 5,* 642-657.

Ikeda, M., 1984, Coastal flows driven by a local density flux, *J. Geophys. Res., 89,* 8008-8016.

Kao, T.W., 1981, The dynamics of ocean fronts. Part I. Shelf water structure due to freshwater discharge, *J. Phys. Oceanogr., 11,* 1215-1223.

_____, C. Park and H.-P. Pao, 1978, Inflows, density currents, and fronts, *Phys. Fluids, 21,* 1912-1922.

Kreiss, H.O., 1966, Difference approximations for the initial boundary value problem for hyperbolic differential equations, in Proc. Symp. at the University Of Wisconsin, May 1966, D. Greenspan, Ed., Wiley

McCreary, J.P., 1983, A model of tropical ocean-atmosphere interaction, *Monthly Weather Review, 111,* 370-387.

O'Donnell, J., 1986, A Numerical Model of the Dynamics of Buoyant Discharges, PhD Dissertation, University of Delaware, Newark, DE, 182pp.

Orlanski, I., 1976, A simple boundary condition for unbounded hyperbolic flows, *J. Comput. Phys., 21,* 251-269.

Roach, P.J., 1976, **Computational Fluid Dynamics,** Hermosa Press, Albuquerque NM, 434pp.

Spaulding, M.L., 1984, A vertically averaged circulation model using boundary-fitted coordinates, *J. Phys. Oceanogr., 14,* 973-982.

Stern, M.E., J.A. Whitehead and B.-L. Hua, 1982, The intrusion of a density current along the coast of a rotating fluid, *J. Fluid Mech., 123,* 237-265.

Wang, D.-P. and D.W. Kravitz, 1980, A semi-implicit two-dimensional model of estuarine circulation, *J. Phys. Oceanogr., 10,* 441-454.

_____, 1985, Numerical study of gravity currents in a channel, *J. Phys. Oceanography, 15,* 299-305.

Webb, A.J. and J.S. Pond, 1986, Propagation of a Kelvin wave around a bend in a channel, *J. Fluid Mech., 169,* 257-274.

Whitehead, J.A. and D.C. Chapman, 1986, Laboratory observations of a fresh water gravity current on a shelf: The generation of shelf waves, *J. Fluid Mech., 172,* 373-399.

APPENDIX A

DERIVATIONS

Governing Equations The model equations are derived from the two layer case as follows.

$$U_{1_t} + L(U_1) - fV_1 = -h_1 P_{1_x} + Ah_1 \nabla^2 u_1 + \tau^x - r_i u_1 \tag{A1}$$

$$V_{1_t} + L(V_1) + fU_1 = -h_1 P_{1_y} + Ah_1 \nabla^2 v_1 + \tau^y - r_i v_1 \tag{A2}$$

$$U_{2_t} + L(U_2) - fV_2 = -h_2 P_{2_x} + Ah_2 \nabla^2 u_2 - \tau_B^x + r_i u_2 \tag{A3}$$

$$V_{2_t} + L(V_2) + fU_2 = -h_2 P_{2_y} + Ah_2 \nabla^2 v_2 - \tau_B^y + r_i v_2 \tag{A4}$$

$$(h_{1_t} + \varepsilon h_1) + U_{1_x} + V_{1_y} = 0 \tag{A5}$$

$$(h_{2_t} + \varepsilon h_2) + U_{2_x} + V_{2_y} = 0 \tag{A6}$$

$$h_1 + h_2 = h_T(x,y) \tag{A7}$$

$$\nabla P_2 = \nabla P_1 + g^* \nabla h_2 \tag{A8}$$

where

L( ) is an operator defining the nonlinear terms (= $[u(\ )]_x + [v(\ )]_y$),
g^* is reduced gravity,
$\tau^{x,y}$ is the wind stress,
r_i is the interfacial drag coefficient,
ε is the Newtonian cooling coefficient, and
subscripts t, x, and y indicate time and space derivatives.

Now, using the assumption of an infinitely deep, inert lower layer, equations (A3) and (A4) vanish and (A6) becomes undefined. This is consistent with the assump-

tion that $h_T = \infty$. Finally, equation (A8) can be rewritten using (A7) as follows

$$\nabla P_1 = -g^* \nabla(h_T - h_1) \tag{A8a}$$

Evaluate ∇h_T as approximately $\Delta h_T/(\Delta x, \Delta y)$. Then assume $\Delta h_T = h_{T_i} - h_{T_{i-1}} \approx 0$, so that $\nabla h_T \approx 0$ and (A8a) becomes

$$\nabla P_1 = -g^* \nabla(-h_1) \tag{A8b}$$

Substitute (A8b) into (A1) and (A2) and rewrite to give

$$U_t + L(U) - fV = -g^* h \eta_x + Ah \nabla^2 u + \tau^x - r_i u \tag{A9}$$

$$V_t + L(V) + fU = -g^* h \eta_y + Ah \nabla^2 v + \tau^y - r_i v \tag{A10}$$

$$\eta_t + \varepsilon\eta + U_x + V_y = 0 \tag{A11}$$

where $\eta = h - h_0$, h_0 a constant.

Momentum Equations on a Boundary Derivation of the interface depth "outside" the physical boundary, using the x-momentum equation as an example, is as follows:

$$-fV = -g^* h h_x + Ah \nabla^2 u + \tau^x - r_i u \tag{A12}$$

divide (A12) by $g^* h$ to give

$$h_x = \frac{fv}{g^*} + \frac{A}{g^*} u_{xx} + \frac{\tau^x}{g^* h} \tag{A13}$$

since u_{yy} and $u \equiv 0$ on the boundary. Next use a Taylor series expansion to get a

second order accurate form for the second partial derivative term.

$$u_{i+1} = u_i + \Delta x u_x|_i + \frac{\Delta x^2}{2!} u_{xx}|_i + \textit{higher order terms} \tag{A14a}$$

$$u_{i+2} = u_i + 2\Delta x u_x|_i + \frac{(2\Delta x)^2}{2!} u_{xx}|_i + \textit{higher order terms} \tag{A14b}$$

Rewrite (A14a) in terms of the first partial and substitute into (A14b) to give

$$\frac{(u_{i+2} + u_i - 2u_{i+1})}{\Delta x^2} = u_{xx}|_i \tag{A14c}$$

Finally, use the fact that on the boundary $u = 0$ to give the form for the momentum equation at a boundary.

$$h_x = \frac{(h_1 - h_0)}{\Delta x} = \frac{fv}{g^*} + \frac{A}{g^*}\frac{(u_3 - 2u_2)}{\Delta x^2} + \frac{\tau^x}{g^* h} \tag{A15}$$

APPENDIX B

EFFECTS OF FRICTION AND DETRAINMENT

Solutions of the linear governing equations were sought to determine an analytical form for the phase speed which included both interfacial friction and Newtonian cooling. These lead to forms for interface height η and velocity of

$$\left[\frac{\partial^2}{\partial t^2} + f^2\right]u + r^{*2}\,u + 2r^*\frac{\partial u}{\partial t} = -g^*\left[f\frac{\partial \eta}{\partial y} + \frac{\partial^2 \eta}{\partial x\,\partial t} + r^*\frac{\partial \eta}{\partial x}\right] \tag{B1}$$

$$\left[\frac{\partial^2}{\partial t^2} + f^2\right]v + r^{*2}\,v + 2r^*\frac{\partial v}{\partial t} = g^*\left[f\frac{\partial \eta}{\partial x} - \frac{\partial^2 \eta}{\partial y\,\partial t} - r^*\frac{\partial \eta}{\partial y}\right] \tag{B2}$$

$$\frac{\partial}{\partial t}\left\{\left[\frac{\partial^2}{\partial t^2} + f^2\right]\eta - C_0^2\nabla^2\eta\right\} + \varepsilon\left\{\left[\frac{\partial^2}{\partial t^2} + f^2\right]\eta + \left[2r^*\frac{\partial}{\partial t} + r^{*2}\right]\eta\right\}$$

$$+ r^*\left\{\left[2\frac{\partial^2}{\partial t^2} + r^*\frac{\partial}{\partial t}\right]\eta - C_0^2\nabla^2\eta\right\} = 0 \tag{B3}$$

where

> r^* the Rayleigh friction coefficient is r_i/h and
> boundary conditions are $v = 0$ on $y = 0, L$.

Assumption that η has the form $\eta_1(y)e^{i(kx - \sigma t)}$ allows (B3) to be written as

$$\eta_{1yy} + \gamma^2\,\eta_1 = 0 \tag{B4}$$

where

$$\gamma^2 = \left[\frac{\sigma + i\varepsilon}{\sigma + ir^*}\right]\left[\frac{\sigma^2 - f^2}{C_0^2} - \frac{r^{*2}}{C_0^2} + \frac{2ir^*\sigma}{C_0^2}\right] - k^2 \tag{B5}$$

Solutions of (B4) have the form $\eta_1 = A\sin\gamma y + B\cos\gamma y$. Using the boundary conditions (B2) becomes

$$\eta_{1y} + \frac{fk}{\sigma + ir^*}\eta_1 = 0 \tag{B6}$$

which, using the form above for η_1, yields a pair of equations whose solution requires that

$$\left[\gamma^2 + \frac{f^2k^2}{(\sigma + ir^*)^2}\right]\sin\gamma L = 0 \tag{B7}$$

Then either the term in parentheses, which leads to the Kelvin wave solution, or the sine term, which yields the Poincaré wave, must be zero.

The term in parentheses reduces to

$$\begin{aligned}&(\sigma^2 - C_0^2k^2 - \varepsilon r^*)(\sigma^2 - f^2 - r^{*2}) - 2\sigma^2(\varepsilon r^* + r^{*2})\\ &+ i\sigma\left[(\varepsilon + r^*)(\sigma^2 - f^2 - r^{*2}) + 2r^*(\sigma^2 - C_0^2k^2 - \varepsilon r^*)\right] = 0\end{aligned} \tag{B8}$$

which, when r* and ε are zero, yields the familiar, linear inviscid form

$$(\sigma^2 - C_0^2k^2)(\sigma^2 - f^2) = 0 \tag{B9}$$

In equation (B5) the effect of detrainment is removed when $r^* \approx \varepsilon$. Indeed it can be shown in this set of circumstances that frequency is complex; the real part is C_0k, the Kelvin wave solution, and the imaginary part is $-r^*$. The implication is that phase speed is unaffected but that energy is dissipated at a rate controlled by

friction. The solution for η is then a damped Kelvin wave of the form

$$\eta(x,y,t) = \eta_0 e^{-y/R_0} e^{-r^* t} \cos(kx - \sigma t) \tag{B10a}$$

$$u(x,y,t) = C_0 \frac{\eta_0}{h_0} e^{-y/R_0} e^{-r^* t} \cos(kx - \sigma t) \tag{B10b}$$

$$v = 0 \tag{B10c}$$

and the exponential decay term ($e^{-r^* t}$) is the only change from the inviscid solution. Solution of the $\sin(\gamma L)$ term has a similar result in that the only difference between the viscid and inviscid forms is the addition of the exponential time decay term.

Inclusion of both detrainment and interfacial friction leads to a form in which, as expected, frequency is complex. Experimental evidence suggested that the real part should be

$$\sigma_R{}^2 = C_0{}^2 k^2 + \Phi(\varepsilon, r^*) \tag{B11a}$$

and the imaginary part

$$\sigma_I{}^2 = \frac{1}{3}\left\{(C_0^2 k^2 + f^2 + r^{*2})\left[1 - \frac{2r^*}{a_1 \sigma_R}\right] + \left[\Phi - \frac{2\varepsilon r^*}{a_1 \sigma_R}\right]\right\} \tag{B11b}$$

where $a_1 = \varepsilon + 3r^*$.

Interfacial (Rayleigh) friction and detrainment are both seen to affect phase speed directly and the decay term is no longer simple.

The situation for the Poincaré wave is similar. The frequency is complex, and assuming the real part is

$$\sigma_R{}^2 = C_0^2\left[k^2 + \frac{n^2\pi^2}{L^2}\right] + \Phi(\varepsilon, r^*) \tag{B12a}$$

the imaginary part is

$$\sigma_I = \sigma_I(\sigma_R, \varepsilon, r^*) \tag{B12b}$$

with the implication, as in the case of the Kelvin wave, that phase speed will either increase or decrease depending on the sign of Φ.

A second approach is to make a long wave approximation in a semi-infinite domain as follows; the governing equations in a coordinate system with a coast at $x = 0$ are

$$fv = g\eta_x \tag{B13a}$$

$$v_t + fu = -g\eta_y - r^*v \tag{B13b}$$

$$\eta_t + \varepsilon\eta = -h_0(u_x + v_y) \tag{B13c}$$

Next assume that v and η are periodic in the along shelf direction and decay exponentially in the cross shelf direction.

$$v(x,y,t) = v_0 e^{i(ly-\sigma t)} e^{-\gamma x} \tag{B14a}$$

and

$$\eta(x,y,t) = \eta_0 e^{i(ly-\sigma t)} e^{-\gamma x} \tag{B14b}$$

Use B14a and B14b in B13 to solve for γ.

$$\frac{r^* + i\sigma}{\varepsilon + i\sigma} = \frac{1}{\gamma^2 R_0^2} \tag{B15}$$

Four possibilities arise with respect to ε and r^*

(a) $\varepsilon = r^* = 0$,

(b) $\varepsilon = r^* \neq 0$,

(c) $\varepsilon = 0, r^* \neq 0$, equivalent to $r^* > \varepsilon$ and

(d) $\varepsilon \neq 0, r^* = 0$, equivalent to $\varepsilon > r^*$.

Case (a) gives $\gamma = R_0^{-1}$, the linear, inviscid Kelvin wave solution. Case (b) has the same form for γ. Use of the boundary condition $u = 0$ on $x = 0$ implies that frequency is complex with $\sigma_R = C_0 l$ and $\sigma_I = -r^*$ with the provision that σ_I could also be written as $-\varepsilon$ or as $-(\varepsilon + r^*)/2$.

Cases (c) and (d) imply both γ and σ are complex. Now, using the complex forms for γ and σ, rewrite η as follows:

$$\eta(x,y,t) = \eta_0 e^{-(\gamma_R x + \sigma_I t)} \cos(ly - \sigma_R t)\cos\gamma_I x \pm \sin(ly - \sigma_R t)\sin\gamma_I x \quad \text{(B16)}$$

where the sign before the sine term is determined by the sign of γ_I. Using B15 it can be shown that $\gamma_I < 0$ for case (c) and $\gamma_I > 0$ for case (d). Thus Rayleigh friction induces phase propagation toward the coast and Newtonian cooling induces phase propagation away from the coast, while both cause temporal and spatial decay of the wave.

APPENDIX C

MODEL FORTRAN CODE

```
1             program bshmod4
2     c
3     c      'bshmod4.1'  5/7/86
4     c  Uses full Orlanski radiation condition on N and S boundaries of shelf.
5     c  Includes 'Newtonian cooling' in continuity equation.
6     c  Size of domain is reduced to 200x300 km. Channel is 20x100 km with
7     c  solid walls on channel and western boundary of shelf.
8     c  Staggered grid system same as Holland-Lin model
9     c  N-S(E-W) boundaries coincide with v(u) points.
10    c  Modified (tjb) 10/85
11    c  This program is executed by a shell program called 'bshmod4.sh'
12    c  which passes frequently changed parameters.
13    c
14            parameter (maxx=100,maxy=150)
15            parameter (maxx1=maxx+1,maxy1=maxy+1)
16            parameter (maxx2=maxx+2,maxy2=maxy+2)
17            dimension u(maxx1,maxy1,3),v(maxx1,maxy1,3),h(maxx1,maxy1,3),
18       1  fu(maxx,maxy),fv(maxx,maxy),fp(maxx,maxy),f(maxy),taux(maxy1),
19       2  tauy(maxy1),s(maxx2,maxy2),q(maxx2,maxy2),
20       3  e(maxx2,maxy2),y(maxy1),ihw(maxx)
21       4  ,hpl(maxx,maxy),ub(maxx,maxy),vb(maxx,maxy),ub1(maxx/2,maxy/2),
22       5  vb1(maxx/2,maxy/2),wf(maxy1)
23       6  ,vt(maxx),ut(maxx),ht(maxx)
24       7  ,vt1(maxx),ut1(maxx),ht1(maxx)
25            character*18,savf,strtf
26            character*10,day
27            character*6,dayn
28            integer sday,eday,d(maxx1,maxy1)
29            real nday
30            data hcut/10020./,radius/6.378e8/
31            data c/125./,beta/2.e-13/,gp/2./,gr/1000./,
32       1  pi/3.1415927/,h0/1000./
33            data xmin/0./,ymin/0./,xmax/2.e7/,ymax/3.e7/
34            data xlen1/8.0/,ylen1/6.0/,xmin1/0./,xmin2/-4./,xmax2/.8/,ymin1/
35       1  1./,ihmax/4/,jhmax/12/
36            data kins/11/,irsn/0/
37            data ibkgrd/0/
38    c       data irsth/0/
39            data kin/10/,kot/11/
40    c--- define wind patch function wf(j)---
41            data (wf(j),j=1,15)/15*0./,(wf(j),j=135,151)/17*0./,(wf(j),j=20
42       1  ,130)/111*1./,wf(16),wf(134)/2*.2/,wf(17),wf(133)/2*.4/,wf(18),
43       2  wf(132)/2*.6/,wf(19),wf(131)/2*.8/
44    c--- read frequently changed parameters --------
45    c
46            read(5,*) nstep1,nstep2
47            read(5,*) isave
48            read(5,*) irstrt
49            read(5,*) timstp
50    c--- read filename used to restart program ----------
51            read(5,'(a18)') strtf
52    c--- read filename where results are stored for restart ---
53            read(5,'(a18)') savf
54    c--- read kchk which determines time between plots ---
```

```
55                read(5,*) kchk
56      c--- read wind amplitudes
57                read(5,*) taux0,tauy0
58      c--- read values for estuarine inflow u0, spin up parameter alpha
59      c--- and spin up on(1) or off(0)
60              read(5,*) u0,v0
61                read(5,*) alpha
62                read(5,*) ispn
63      c--- read contour interval and min vector to plot ----------
64                read(5,*) cntrl,umin
65      c--- read A, Newtonian cooling coeff. and Interfacial friction coeff.
66                read(5,*) a,eps,fnu
67      c-------------------------------------------------------------------
68                nx=maxx
69                ny=maxy
70      c  na is total number of gridpoints
71              na=nx*ny
72                sday=nstep1*timstp/86400.+.5
73                eday=nstep2*timstp/86400.+.5
74      c
75                print 1700,nx,ny,sday,eday,timstp,a,eps,fnu,gp,u0,v0,savf
76       1700     format(10x,'Berger Circulation Model',//
77          1  ,1x,'Grid size=',i5,' by',i5,5x,i5,' to',i5,' days',/,1x,
78          2  'Time step (secs)=',f10.3,/,1x,'A=',e9.1,3x,'eps=',e9.1,/
79          3  ,1x,'Interfacial friction=',f8.4,1x,'g*=',f4.2,/
80          4  ,1x,'U0=',f6.2,1x,'V0=',f6.2,/,1x,a18)
81
82                iwhich=2
83                lstdne=0
84                iptt=0
85                nxp1=nx+1
86                nyp1=ny+1
87                nxp2=nx+2
88                nyp2=ny+2
89                nym1=ny-1
90                nxm1=nx-1
91                xdis=xmax-xmin
92                dx=xdis/float(nx)
93                ydis=ymax-ymin
94                dy=ydis/float(ny)
95                dxi=1./dx
96                dyi=1./dy
97                dxi2=dxi*dxi
98                dyi2=dyi*dyi
99                ymid=(ymax+ymin)/2.
100               agx=a/gp/dx
101               agy=a/gp/dy
102               gp2=gp/2.
103               gpi=1./gp
104               gri=1./gr
105     c         sig=2.*pi/(ccccc)
106               dt=timstp
107     c--- set bit map used to mask area.
108               do 90 j=1,nyp1
109               do 90 i=1,nxp1
110               if (i.ge.51) then
111                       d(i,j)=1
112               else if (i.lt.51 .and. j.lt.101 .or. j.ge.111) then
113                       d(i,j)=0
114                   else
115                       d(i,j)=1
116               endif
117        90     continue
118     c         do 91 j=nyp1,1,-1
```

```
c 91     write(6,119) (d(i,j),i=1,nxp1)
c 119      format(1x,101i1)
c
c--- Define boundary conditions: -= free-slip, += no-slip
c                              in vface/w & ufacs/n
              uvfac=2.*a*(dxi2+dyi2)
c--- fnu represents interfacial friction  ( zero in this mod )
c
              ufacs=uvfac+a*dyi2
              ufacn=ufacs
              vface=uvfac-a*dxi2
              vfacw=uvfac+a*dxi2
c
c--- Compute Coriolis parameter
c
c             do 31 j=1,nyp1
c  31         y(j)=ymin+(j-.5)*dy
c             omega=2.*pi/86400.
              do 30 j=1,ny
c  30         f(j)=2.*omega*sin(y(j)/radius)
   30   f(j)=1.e-4
c
c--- Initialize u,v,h, and wind field
c
c             u,v interior
              do 32 j=1,ny
              do 32 i=2,nx
              u(i,j,1)=0.
   32         u(i,j,2)=0.
              do 33 j=2,ny
              do 33 i=1,nx
              v(i,j,1)=0.
   33         v(i,j,2)=0.
              do 331 j=2,ny
  331         v(1,j,3)=0.
c u,v on boundaries
              do 35 j=1,ny
              u(1,j,2)=0.
              u(1,j,3)=0.
              u(nxp1,j,2)=0.
              u(nxp1,j,3)=0.
    35    fu(1,j)=0.
              do 351 j=1,100
              u(51,j,2)=0.
              u(51,j,3)=0.
   351        fu(51,j)=0.
              do 352 j=111,ny
              u(51,j,2)=0.
              u(51,j,3)=0.
   352        fu(51,j)=0.
              do 36 i=1,nx
              v(i,1,1)=0.
              v(i,1,2)=0.
    36    fv(i,1)=0.
              do 360 i=1,50
              v(i,nyp1,1)=0.
   360        v(i,nyp1,2)=0.
              do 361 i=1,50
              v(i,101,3)=0.
              v(i,111,3)=0.
              fv(i,101)=0.
   361        fv(i,111)=0.
c             do 363 i=51,nx
c             v(i,nyp1,1)=v0
```

```
c           v(i,nyp1,2)=v0
c 363       v(i,nyp1,3)=v0
c--- Open file needed by GKS ( ncar Graphics Kernel System)
            open (3,file='/ocean/ocean/lib/pwritx.dat',status='old')
c--- Initial run(irstrt=0) or restart(irstrt=1) from previous run -----
            if (irstrt.eq.0) go to 16
            la=mod(nstep1-1,3)+1
            l =mod(nstep1  ,3)+1
c
            open (kin,file='/ocean/berger/results/'//strtf,status='unknown')
            do 17 j=1,ny
 17     read (kin,111) (u(i,j,la),i=1,nxp1)
            do 57 j=1,ny
 57     read (kin,111) (u(i,j,l),i=1,nxp1)
            read (kin,111) (ut(i),i=1,nx)
            read (kin,111) (ut1(i),i=1,nx)
            do 18 j=1,nyp1
 18     read (kin,111) (v(i,j,la),i=1,nx)
            do 58 j=1,nyp1
 58     read (kin,111) (v(i,j,l),i=1,nx)
            read (kin,111) (vt(i),i=1,nx)
            read (kin,111) (vt1(i),i=1,nx)
            do 19 j=1,ny
 19         read (kin,111) (h(i,j,la),i=1,nx)
            do 59 j=1,ny
 59         read (kin,111) (h(i,j,l),i=1,nx)
            read (kin,111) (ht(i),i=1,nx)
            read (kin,111) (ht1(i),i=1,nx)
            close (kin)
 111    format(51e16.8)
            go to 25
c initialize h
 16     continue
            do 34 j=1,nyp1
            do 34 i=1,nxp1
            h(i,j,1)=h0
 34     h(i,j,2)=h0
c--- initialize ut, vt, ht
            do 340 i=1,nx
            ut(i)=0.
            vt(i)=0.
          ht(i)=h0
            ut1(i)=0.
            vt1(i)=0.
 340    ht1(i)=h0
c
  25    write(6,101)
 101        format(' Initial h field(m) every 10th x & y',/)
            do 50 j=ny,1,-10
            do 51 i=1,nx,10
  51        ihw(i)=h(i,j,2)/100.+.5
            write(6,102) (ihw(i),i=1,nx,10)
  50        continue
 102    format(15i4)
            do 341 j=1,ny
            do 341 i=1,nx
 341    fp(i,j)=0.
c
            itt=nstep1-1
            sumt=0.
c
c--- Define wind stress field: taux=taux0*wf(j) (+=W in met sense)
c                              tauy=tauy0*wf(j) (+=S in met sense)
c   note: move wind stress definition inside loop 20
```

```
c         if wind stress is function of time.
            do 83 j=1,nyp1
            taux(j)=taux0*wf(j)
            tauy(j)=tauy0*wf(j)
 83   continue
c--- open graphics workstation------
            call opngks
c
            k=nstep1
            if (irstrt.eq.1) then
                  k1=nstep1
            else
                  k1=1
            endif
c-------------------TIME STEP -----------------------------------
 200        if(k.gt.nstep2) go to 201
c--- check whether to spin up inflow velocity---
            if(ispn.eq.1) then
                  tat=2.+u0*tanh(alpha*k1*dt)
            else
                  tat=u0
            endif
c
            do 356 j=101,110
            u(1,j,1)=tat
            u(1,j,2)=tat
            u(1,j,3)=tat
 356        continue
c
            time1=float(nstep1*dt)
c
c--- Begin u,v,p calculations
c
            itt=itt+1
            la=mod(itt-1,3)+1
            l= mod(itt  ,3)+1
            lb=mod(itt+1,3)+1
c
c la= last , l= present , lb= future
c
            marker=2
c--- Euler backward timestep every 53 steps
c note backward timestep at a prime number of steps
c
            if (mod(itt,53).ne.1) go to 21
            marker=1
            do 1 j=1,nyp1
            do 1 i=1,nxp1
            u(i,j,la)=u(i,j,l)
            v(i,j,la)=v(i,j,l)
  1         h(i,j,la)=h(i,j,l)
 21         deltat=marker*dt
c
c define u(old),v(old) and h outside boundaries
c u(old)=q, v(old)=e and h=s
c
  2         do 1001 j=2,nyp1
            do 1001 i=2,nxp1
            q(i,j)=u(i-1,j-1,la)
            e(i,j)=v(i-1,j-1,la)
1001        s(i,j)=h(i-1,j-1,l)
            do 1002 i=2,nxp1
            q(i,1)=0.
            q(i,nyp2)=0.
```

```
311   c wall depth on S(j=1) and N(j=nyp2) 'open' boundaries
312                 s(i,1)=h(i-1,1,l)
313    1002         s(i,nyp2)=h(i-1,ny,l)
314                 do 1003 j=2,nyp1
315                 e(1,j)=0.
316                 e(nxp2,j)=0.
317   c wall depth on W(i=1) 'open' boundary
318                 s(1,j)=h(1,j-1,l)
319   c wall depth on E(i=nxp2) 'free slip' boundary
320    1003         s(nxp2,j)=agx*(u(nxm1,j,la)-2.*u(nx,j,la))+h(nx,j-1,l)
321       1            +f(j)*dx*gpi*.5*(v(nx,j+1,l)+v(nx,j,l))
322       2            +taux(j-1)*dx*gpi/h(nx,j-1,l)
323                 do 1004 i=2,50
324                 q(i,101)=0.
325                 q(i,112)=0.
326   c wall depth on S(j=101) channel boundary - 'no slip'
327                 s(i,101)=-agy*(v(i,103,la)-2.*v(i,102,la))+h(i-1,101,l)
328       2            +tauy(101)*dy*gpi/h(i-1,101,l)
329   c wall depth on N(j=111) channel boundary - 'no slip'
330    1004         s(i,112)=agy*(v(i,109,la)-2.*v(i,110,la))+h(i-1,110,l)
331       2            -tauy(110)*dy*gpi/h(i-1,110,l)
332                 do 1005 j=2,101
333                 e(51,j)=0.
334   c wall depth on W(i=51) shelf boundary - 'no slip'
335   c includes corners satisfying x-momentum equation
336    1005         s(51,j)=-agx*(u(53,j,la)-2.*u(52,j,la))+h(51,j-1,l)
337       2            -taux(j-1)*dx*gpi/h(51,j-1,l)
338                 do 1006 j=112,nyp1
339                 e(51,j)=0.
340    1006         s(51,j)=-agx*(u(53,j,la)-2.*u(52,j,la))+h(51,j-1,l)
341       2            -taux(j-1)*dx*gpi/h(51,j-1,l)
342   c--- compute values in the interior
343   c
344                 do 3 j=1,ny
345                 do 3 i=2,nx
346                 if (d(i,j).eq.0) goto 3
347                 fu(i,j)=.25*f(j)*((v(i,j+1,l)+v(i,j,l))*s(i+1,j+1)+
348        1  (v(i-1,j+1,l)+v(i-1,j,l))*s(i,j+1))-gp2*dxi*(s(i+1,j+1)-
349        2  s(i,j+1))*(s(i+1,j+1)+s(i,j+1))+.5*a*(h(i,j,la)+h(i-1,j,la))*
350        3  (dxi2*(q(i+2,j+1)+q(i,j+1))+dyi2*(q(i+1,j+2)+q(i+1,j)))+taux(j)
351   c     4  -.125*dxi*(((s(i+2,j+1)+s(i+1,j+1))*u(i+1,j,l)+(s(i+1,j+1)+
352   c     5  s(i,j+1))*u(i,j,l))*(u(i+1,j,l)+u(i,j,l))-((s(i+1,j+1)+
353   c     6  s(i,j+1))*u(i,j,l)+(s(i,j+1)+s(i-1,j+1))*u(i-1,j,l))*
354   c     7  (u(i,j,l)+u(i-1,j,l)))-.125*dyi*(((s(i+1,j+2)+s(i+1,j+1))*
355   c     8  v(i,j+1,l)+(s(i,j+2)+s(i,j+1))*v(i-1,j+1,l))*(u(i,j+1,l)+
356   c     9  u(i,j,l))-((s(i+1,j+1)+s(i+1,j))*v(i,j,l)+(s(i,j+1)+s(i,j))*
357   c     1  v(i-1,j,l))*(u(i,j,l)+u(i,j-1,l)))
358         2  -fnu*u(i,j,la)
359       3     continue
360   c
361   c--- reset corner values to satisfy y momentum equation
362                 s(51,101)=-agy*(v(51,103,la)-2.*v(51,102,la))+h(50,101,l)
363       1            +tauy(101)*dy*gpi/h(50,101,l)
364                 s(51,112)=agy*(v(51,109,la)-2.*v(51,110,la))+h(50,110,l)
365       1            -tauy(110)*dy*gpi/h(50,110,l)
366   c
367                 do 4 j=2,ny
368                 do 4 i=1,nx
369                 if (d(i,j).eq.0) goto 4
370                 fv(i,j)=-.25*(f(j)*(u(i+1,j,l)+u(i,j,l))*s(i+1,j+1)+f(j-1)*
371        1  (u(i+1,j-1,l)+u(i,j-1,l))*s(i+1,j))-gp2*dyi*(h(i,j,l)-h(i,j-1,l)
372        2  )*(s(i+1,j+1)+s(i+1,j))+.5*a*(h(i,j,la)+h(i,j-1,la))*(dxi2*
373        3  (e(i+2,j+1)+e(i,j+1))+dyi2*(e(i+1,j+2)+e(i+1,j)))+tauy(j)
374   c     4  -.125*dxi*(((s(i+1,j+1)+s(i+2,j+1))*u(i+1,j,l)+(s(i+1,j)+
```

```
c     5     s(i+2,j))*u(i+1,j-1,l))*(v(i+1,j,l)+v(i,j,l))-((s(i,j+1)+
c     6  s(i+1,j+1))*u(i,j,l)+(s(i,j)+s(i+1,j)
c     7  )*u(i,j-1,l))*(v(i,j,l)+v(i-1,j,l)))-.125*dyi*(((s(i+1,j+2)+
c     8  s(i+1,j+1))*v(i,j+1,l)+(s(i+1,j+1)+s(i+1,j))*v(i,j,l))*
c     9  (v(i,j+1,l)+v(i,j,l))-((s(i+1,j+1)+s(i+1,j))*v(i,j,l)+
c     1  (s(i+1,j)+s(i+1,j-1))*v(i,j-1,l))*(v(i,j,l)+v(i,j-1,l)))
      2  -fnu*v(i,j,la)
  4     continue
c
            do 5 j=1,ny
            do 5 i=1,nx
            if (d(i,j).eq.0) goto 5
            fp(i,j)=-.5*(dxi*((s(i+2,j+1)+s(i+1,j+1))*u(i+1,j,l)-(s(i+1,j+1)
     1  +s(i,j+1))*u(i,j,l))+dyi*((s(i+1,j+2)+s(i+1,j+1))*v(i,j+1,l)-
     2  (s(i+1,j+1)+s(i+1,j))*v(i,j,l)))
  5         continue
c
        do 6 j=2,nym1
            do 6 i=1,nx
            h(i,j,lb)=h(i,j,la)+deltat*(fp(i,j)-eps*(h(i,j,la)-h0))
  6     continue
            do 66 i=1,nx
            ah=h(i,2,l)+ht(i)-2.*h(i,3,la)
            if (ah.eq.0.) then
              h(i,1,lb)=h0
              goto 66
            else
              clh=(ht(i)-h(i,2,l))/ah
            endif
            if (clh.le.0.) then
              h(i,1,lb)=h(i,1,la)
            else if (clh.ge.1.) then
              h(i,1,lb)=h(i,2,l)
            else
              h(i,1,lb)=(h(i,1,la)*(1.-clh)+2.*clh*h(i,2,l))/(1.+clh)
            endif
 66         continue
            do 661 i=1,nx
            ah1=h(i,nym1,l)+ht1(i)-2.*h(i,ny-2,la)
            if (ah1.eq.0.) then
              h(i,ny,lb)=h0
              goto 661
            else
              clh1=(ht1(i)-h(i,nym1,l))/ah1
            endif
            if (clh1.le.0.) then
              h(i,ny,lb)=h(i,ny,la)
            else if (clh1.ge.1.) then
              h(i,ny,lb)=h(i,nym1,l)
            else
              h(i,ny,lb)=(h(i,ny,la)*(1.-clh1)
     1                +2.*clh1*h(i,nym1,l))/(1.+clh1)
            endif
 661        continue
            do 61 i=1,50
            h(i,111,lb)=h0
 61         h(i,100,lb)=h0
c
c--- Compute U in interior
c
            uvfac1=.5*(1.-deltat*uvfac)
            do 10 j=2,nym1
            do 10 i=2,nx
            if (d(i,j).eq.0) goto 10
```

```
439                 u(i,j,lb)=uvfac1*u(i,j,la)*(h(i,j,la)+h(i-1,j,la))+deltat*
440       1                   fu(i,j)
441        10   continue
442       c--- Reset u on western shelf boundary
443                 do 1011 j=1,100
444        1011     u(51,j,lb)=0.
445                 do 1021 j=111,ny
446        1021     u(51,j,lb)=0.
447       c--- Note: u on open boundary = u(interior)
448       c--- unless boundary has inflow, then u=0
449                 do 11 i=52,nx
450                 au=u(i,2,l)+ut(i)-2.*u(i,3,la)
451                 if (au.eq.0.) then
452                   u(i,1,lb)=0.
453                   goto 11
454                 else
455                   clu=(ut(i)-u(i,2,l))/au
456                 endif
457                 if (clu.le.0.) then
458                   u(i,1,lb)=u(i,1,la)
459                 else if (clu.ge.1.) then
460                   u(i,1,lb)=u(i,2,l)
461                 else
462                   u(i,1,lb)=(u(i,1,la)*(1.-clu)+2.*clu*u(i,2,l))/(1.+clu)
463                 endif
464        11       continue
465                 do 110 i=52,nx
466                 u(i,ny,lb)=0.
467                 au1=u(i,nym1,l)+ut1(i)-2.*u(i,ny-2,la)
468                 if (au1.eq.0.) then
469                   u(i,ny,lb)=0.
470                   goto 110
471                 else
472                   clu1=(ut1(i)-u(i,nym1,l))/au1
473                 endif
474                 if (clu1.le.0.) then
475                   u(i,ny,lb)=u(i,ny,la)
476                 else if (clu1.ge.1.) then
477                   u(i,ny,lb)=u(i,nym1,l)
478                 else
479                   u(i,ny,lb)=(u(i,ny,la)*(1.-clu1)
480       1                         +2.*clu1*u(i,nym1,l))/(1.+clu1)
481                 endif
482        110      continue
483       c
484       c compute U on channel boundaries
485       c
486                 ufacs1=.5*(1.-deltat*ufacs)
487                 ufacn1=.5*(1.-deltat*ufacn)
488                 do 112 i=2,51
489                 u(i,101,lb)=ufacs1*u(i,101,la)*(h(i,101,la)+h(i-1,101,la))+
490       1                   deltat*fu(i,101)
491               u(i,110,lb)=ufacn1*u(i,110,la)*(h(i,110,la)+h(i-1,110,la))+
492       1                   deltat*fu(i,110)
493        112    continue
494       c
495       c compute V in interior
496       c
497                 do 12 j=2,ny
498                 do 12 i=2,nxm1
499                 if (d(i,j).eq.0) goto 12
500                   v(i,j,lb)=uvfac1*v(i,j,la)*(h(i,j,la)+h(i,j-1,la))+deltat*
501       1               fv(i,j)
502        12   continue
```

```
503     c
504     c compute V on E & W boundaries
505                 vfacw1=.5*(1.-deltat*vfacw)
506                 vface1=.5*(1.-deltat*vface)
507                 do 13 j=2,ny
508       13    v(nx,j,lb)=vface1*v(nx,j,la)*(h(nx,j,la)+h(nx,j-1,la))+deltat*
509           1           fv(nx,j)
510     c
511                 do 131 j=2,101
512       131       v(51,j,lb)=vfacw1*v(51,j,la)*(h(51,j,la)+h(51,j-1,la))+
513           1             deltat*fv(51,j)
514                 do 132 j=111,ny
515       132       v(51,j,lb)=vfacw1*v(51,j,la)*(h(51,j,la)+h(51,j-1,la))+
516           1             deltat*fv(51,j)
517                 do 133 i=1,50
518                 v(i,101,lb)=0.
519       133       v(i,111,lb)=0.
520     c
521     c compute v on N and S, i.e.'open', boundaries
522     c
523           do 145 i=51,nx
524                 av=v(i,2,l)+vt(i)-2.*v(i,3,la)
525                 if (av.eq.0.) then
526                   v(i,1,lb)=0.
527                   goto 145
528                 else
529                   clv=(vt(i)-v(i,2,l))/av
530                 endif
531                 if (clv.le.0.) then
532                   v(i,1,lb)=v(i,1,la)
533                 else if (clv.ge.1.) then
534                   v(i,1,lb)=v(i,2,l)
535                 else
536                   v(i,1,lb)=(v(i,1,la)*(1.-clv)+2.*clv*v(i,2,l))/(1.+clv)
537                 endif
538       145       continue
539           do 1451 i=51,nx
540                 av1=v(i,ny,l)+vt1(i)-2.*v(i,nym1,la)
541                 if (av1.eq.0.) then
542                   v(i,nyp1,lb)=0.
543                   goto 1451
544                 else
545                   clv1=(vt(i)-v(i,ny,l))/av1
546                 endif
547                 if (clv1.le.0.) then
548                   v(i,nyp1,lb)=v(i,nyp1,la)
549                 else if (clv1.ge.1.) then
550                   v(i,nyp1,lb)=v(i,ny,l)
551                 else
552                   v(i,nyp1,lb)=(v(i,nyp1,la)*(1.-clv1)
553           1                         +2.*clv1*v(i,ny,l))/(1.+clv1)
554                 endif
555       1451      continue
556     c
557                 do 23 j=2,nym1
558                 do 23 i=2,nx
559                 if (d(i,j).eq.0) goto 23
560                 u(i,j,lb)=2*u(i,j,lb)/(h(i,j,lb)+h(i-1,j,lb))
561        23     continue
562                 do 24 j=2,ny
563                 do 24 i=1,nx
564                 if (d(i,j).eq.0) goto 24
565               v(i,j,lb)=2*v(i,j,lb)/(h(i,j,lb)+h(i,j-1,lb))
566        24       continue
```

```
567               do 88 i=51,nx
568               ut1(i)=u(i,nym1,la)
569               vt1(i)=v(i,ny,la)
570               ht1(i)=h(i,nym1,la)
571               ut(i) =u(i,2,la)
572               vt(i) =v(i,2,la)
573      88     ht(i) =h(i,2,la)
574     c
575               if (marker.eq.2) go to 9
576               if (marker.eq.0) go to 7
577               la=mod(itt  ,3)+1
578               l =mod(itt+1,3)+1
579               lb=mod(itt+2,3)+1
580               marker=0
581               go to 2
582      7        do 8 j=1,nyp1
583               do 8 i=1,nxp1
584               u(i,j,l)=u(i,j,lb)
585               v(i,j,l)=v(i,j,lb)
586      8        h(i,j,l)=h(i,j,lb)
587     c
588     c calculate new h if necessary
589     c
590      9        continue
591     c
592               time2=float(k*dt)
593               sumt=time2-time1
594     c
595     c  contour sea surface or velocities every (kchk) hours
596     c
597            if(mod(k,kchk).eq.0) go to 46
598      910      continue
599     c  periodically check if still running and compute avg vertical
600     c  velocity of interface
601               if (mod(k,kchk*2).ne.0) go to 20
602               write(6,907) k,time2/3600.,sumt/3600.
603      907   format(' k=',i5,' ok up to time(hrs):',f6.1,/,
604        1        ' elapsed time this run:',f6.1)
605               sumh=0.
606               do 904 j=1,ny
607               do 904 i=1,nx
608      904      sumh=sumh+h(i,j,lb)-h0
609     c--- adjust na by number of points in masked area
610               sumh=sumh/(na-7000)
611               write(6,903) sumh
612      903      format(' sum of h-h0=',e12.7)
613      20       k=k+1
614               k1=k1+1
615     c  next timestep
616               go to 200
617     c---------------------------- END TIME STEP ----------------------
618      201   k=nstep2
619               lstdne=1
620     c--- save results for future runs
621               if (isave.eq.0) go to 46
622      909      continue
623               open (kot,file='/ocean/berger/results/'//savf,status='unknown')
624     c
625               write(6,998) k
626      998      format(' save u,v,p at timestep ',i7)
627               do 37 j=1,ny
628       37      write (kot,111) (u(i,j,l),i=1,nxp1)
629               do 47 j=1,ny
630       47      write (kot,111) (u(i,j,lb),i=1,nxp1)
```

```
631               write (kot,111) (ut(i),i=1,nx)
632               write (kot,111) (ut1(i),i=1,nx)
633               do 38 j=1,nyp1
634      38       write (kot,111) (v(i,j,l),i=1,nx)
635               do 48 j=1,nyp1
636      48       write (kot,111) (v(i,j,lb),i=1,nx)
637               write (kot,111) (vt(i),i=1,nx)
638               write (kot,111) (vt1(i),i=1,nx)
639               do 39 j=1,ny
640      39     write (kot,111) (h(i,j,l),i=1,nx)
641               do 49 j=1,ny
642      49       write (kot,111) (h(i,j,lb),i=1,nx)
643               write (kot,111) (ht(i),i=1,nx)
644               write (kot,111) (ht1(i),i=1,nx)
645     c
646               if(isave.eq.1) endfile (kot)
647     c
648      46     nday=time2/86400.
649               write (dayn,'(f6.2)') nday
650     c         read (5,'(a6)') dayn
651               day='Day '//dayn
652               iptt=iptt+1
653               if(lstdne.eq.1) go to 999
654     c--- determine interface height relative to h0
655               do 56 j=1,ny
656               do 56 i=1,nx
657               hpl(i,j)=h(i,j,lb)-h0
658               if (hpl(i,j).le.10.) then
659                        hpl(i,j)=0.
660               endif
661      56       continue
662     c--- average u and v to put each at same point as h,
663     c--- then select every other point for plotting
664               do 700 j=1,ny
665               do 700 i=1,nx
666               ub(i,j)=.5*(u(i,j,lb)+u(i+1,j,lb))
667      700      vb(i,j)=.5*(v(i,j,lb)+v(i,j+1,lb))
668               ll=1
669               do 800 j=1,ny/2
670               kk=1
671               do 799 i=1,nx/2
672               ub1(i,j)=ub(kk,ll)
673               vb1(i,j)=vb(kk,ll)
674               kk=kk+2
675      799    continue
676               ll=ll+2
677      800      continue
678     c  Plotting routines for velocity and interface height start here
679     c--- define viewport
680               call set (.2,.8,.1,.95,0.,200.,0.,300.,1)
681     c--- plot interface height relative to h0
682               call conrec (hpl,nx,nx,ny,0.,0.,cntrl,-1,-1,-2)
683     c--- draw perimeter, channel outline and label
684               call labmod ('(f4.0)','(f4.0)',4,4,10,10,0,0,0)
685               call perim (2,5,3,5)
686               call line ( 0.,200.,100.,200.)
687               call line (100.,200.,100., 0.)
688               call line ( 0.,220.,100.,220.)
689               call line (100.,220.,100.,300.)
690               call wtstr (50.,70.,'BAY-SHELF MODEL',14,0,0)
691               call wtstr (50.,60.,'Interface height',10,0,0)
692               call wtstr (50.,55.,'deviation (h-h0)(cm)',10,0,0)
693               call wtstr (50.,45.,day,10,0,0)
694               call wtstr (50.,15.,savf,10,0,0)
```

```
695               call frame
696     c--- plot velocity vectors
697               call velvct (ub1,nx/2,vb1,nx/2,nx/2,ny/2,umin,-1.,-1,50,0,0)
698     c
699               call gperim (2,0,3,0)
700               call line ( 0.,200.,100.,200.)
701               call line (100.,200.,100., 0.)
702               call line ( 0.,220.,100.,220.)
703               call line (100.,220.,100.,300.)
704               call wtstr (50.,70.,'BAY-SHELF MODEL',14,0,0)
705               call wtstr (50.,60.,'Currents (cm/s)',10,0,0)
706               call wtstr (50.,50.,day,10,0,0)
707               call wtstr (50.,15.,savf,10,0,0)
708               call frame
709     c
710               if(lstdne.eq.1) go to 999
711               go to 910
712      999      continue
713     c
714               call clsgks
715               close(3)
716               write(6,1075) isave,irstrt,nstep1,nstep2,savf
717      1075   format(' Parameters at end of this run',/,
718         1           ' isave=',i1,11x,'irstrt=',i1,/,
719         2           ' nstep1=',i10,' nstep2=',i10,/,
720         3         ' savf=',a18)
721     c
722               end
723     c ------------------------------------------------
724               logical function intt(r)
725               real  r
726               if (r.eq.ifix(r)) then
727                         intt=.true.
728               else
729                         intt=.false.
730               endif
731               end
```

AUTOBIOGRAPHICAL STATEMENT

Thomas Joseph Berger

Born:

March 20, 1938; Richardton, North Dakota

Education:

A.B. June 1959, The Catholic University of America
M.S. April 1970, Naval Postgraduate School

Honors:

Sigma Xi, 1959
Phi Kappa Phi, 1985

Appointments and Positions:

U.S. Navy. Commissioned as Ensign in September 1961, retired as Commander in November 1981.
Analysis and Technology, Inc. Senior Analyst December 1981 to December 1982.
Old Dominion University. Research Assistant 1985-1987.

Publications:

Berger, T.J., W.S. Chandler, C.S. Kim and L.P. Atkinson, *SPREX Preliminary Hydrographic Data Report*, Old Dominion University Research Foundation Technical Report 86-1, pp105, June 1986.

_____,_____,_____,_____, *SPREX Hydrographic Data Report*, Vol. 2, Cape Hatteras, Old Dominion University Research Foundation Technical Report 87-1, pp57, January 1987.

T.J. Berger and C.H. Blair, Jr., Effects of Dredging on the Bay Plume, in *Environmental Assessment of Thimble Shoal Channel Borrow Site*, Applied Marine Research Laboratory Report to the Virginia Department of Highways and Transportation, September 1984.

Johnson, D.R. and T.J. Berger, Rapid Boundary Current Meter, in *Applications of Real-Time Oceanographic Circulation Modelling Symposium Proceedings*, ed. B.B. Parker, MTS, Washington DC. pp153-160, 1986.

T.J.Berger and L.P. Atkinson, Oceanographic Observations during GALE, *EOS, Trans. Am. Geophys. U., 67*, p1023, 1986.